Fall 2019

Improvements in digital image correlation and application in material mechanical test

Yunlu Zhang

Department: Mechanical and Aerospace Engineering

IMPROVEMENTS IN DIGITAL IMAGE CORRELATION AND APPLICATION IN MATERIAL MECHANICAL TEST

by

YUNLU ZHANG

A DISSERTATION

Presented to the Graduate Faculty of the

MISSOURI UNIVERSITY OF SCIENCE AND TECHNOLOGY

In Partial Fulfillment of the Requirements for the Degree

DOCTOR OF PHILOSOPHY

in

MECHANICAL ENGINEERING

2019

Approved by

Frank Liou, Advisor
K. Chandrashekhara
Heng Pan
Lianyi Chen
Joseph Newkirk

PUBLICATION DISSERTATION OPTION

This dissertation consists of the following three articles which have been submitted for publication, or will be submitted for publication as follows:

Paper I: Pages 11-38 have been published in Optics and Laser in Engineering.

Paper II: Pages 39-61 have been published in SN Applied Sciences.

Paper III: Pages 62-82 have been accepted to be published in The Journal of Strain Analysis for Engineering Design.

ABSTRACT

Digital image correlation (DIC) is a non-contact full-field optical measurement method. With the advantages of high accuracy, low cost, and simple implementation, it has been widely applied in the area of experimental mechanics. In this study, DIC algorithm has been improved in the aspects of the pixel-level searching method and reference frame update strategy. The feature matching based method is proposed to provide an initial guess for all points of interest with semi-subpixel level accuracy in cases with small or large translation, deformation, or rotation. The bisection searching strategy is presented to automatically adjust the frame step for varying practical circumstances.

The improved DIC algorithm is implemented and applied to the miniature tensile test. A convenient experimental method to determine the true stress-strain curve is proposed. The instantaneous cross-section area is estimated by only one camera in aid of DIC method. The derived true stress-strain curves and mechanical parameters of metal material Al6061 and CP-Ti from miniature specimens match well with the results of standard specimens, and no dimension dependence has been observed in the results.

ACKNOWLEDGMENTS

First and foremost, I would like to express my deep appreciation to my advisor, Dr. Frank Liou, for his encouragement, insightful guidance, and support during my Ph.D. study at Missouri University of Science and Technology. His diligence and rigorous altitude to research and work will have a significant influence on my life. It has been a privilege and a great honor to have worked with him.

I would also like to extend my appreciation to all my dissertation committee members, Dr. K. Chandrashekhara, Dr. Heng Pan, Dr. Lianyi Chen, and Dr. Joseph Newkirk. Without their guidance and valuable comments, it would have been impossible for me to complete my dissertation.

I would like to express my deep thanks to my lab-mates and friends, Dr. Lei Yan, Dr. Sreekar Karnati, Dr. Xueyang Chen, Dr. Jingwei Zhang, Dr. Wei Li, Dr. Xinchang Zhang, Mr. Todd Sparks, Mr. Connor L. Coward, Mr. Yitao Chen, Ms. Wenyuan Cui, Ms. Tan Pan, Dr. Wenbin Li, and Dr. Wei Wang for their support during my study in Rolla.

Last but not least, I wish to extend my special and sincere thanks to my girlfriend, Yuxi Qi, my parents, Mr. Jiangang Zhang and Ms. Yan Huang, and all my family members for their love and unwavering support.

TABLE OF CONTENTS

Page

LIST OF ILLUSTRATIONS

LIST OF TABLES

SECTION

1. INTRODUCTION

1.1. BACKGROUND

Mechanical testing is an indispensable process in material development and manufacturing. Although various standardized specimens are widely adopted in academia and industry, extensive research has been devoted to the mechanical test of miniature specimens. The unique characteristics of the miniature mechanical test require specialized experimental techniques. The aim of this dissertation is to extend the capability of miniature testing with the aid of the non-contact optical metrology method digital image correlation (DIC).

1.1.1. Miniature Mechanical Test. There is a growing interest in the mechanical test of miniature specimens and determining the mechanical properties. The use of miniature specimens could provide several advantages and avoid a few limitations in comparison with conventional specimens. First, the microscale mechanics of material and performance of microcomponents could be directly studied [20]. It is also a valuable tool for evaluating the local properties of inhomogeneous materials like weldment [29] and functional gradient material [23]. Another big motivation comes from the limited volume of the investigated material. To semi-nondestructively evaluate the mechanical properties of the in-service component, the size and shape of available material are much restricted. The nuclear research community also prefers the miniature specimen to reduce the radiological dose from the activated material and efficiently use of costly reactor space [14, 17, 18, 26].

Various types of miniature specimens have been proposed for tensile test, fracture toughness test, flexural test [14], and punch/bulge test [69]. The current research is focused on the miniature tensile test. However, the improvement of the DIC method can be readily applied in other mechanical tests.

The introduction of miniature specimens caused the question about whether the determined mechanical properties are comparable with the results from the conventional specimen, e.g., the scale effect. Over past 20 years, multiple different designs of miniature tensile specimens have been proposed [7, 17, 18, 26, 27, 28, 55, 78]. They feature different dimensions of the gauge section, aspect ratio of the cross-section, radius of the fillet, and gripping mechanism. One conclusion could be drawn from the results of various miniature tensile tests: the determined yield strength, ultimate strength, and uniform elongation are comparable to the standard specimen results. Chen *et al.* [7] concluded that the yield strength of the CuAl7 alloy decreased with increasing thickness then stabilized when the thickness was larger than 0.5 mm. The yield strength is nearly constant when the ratio of thickness t to grain size d is larger than a critical value (about 21). This is coincident with [28], in which the critical ratio was 16, 3.4 and 1.5 for 20MnMoNi55, CrMoV and SS304LN, respectively.

1.1.2. Optical Measurement Technique. Traditionally, surface deformation measurement techniques used in mechanical testing are contact methods such as the electrical strain gauge and the extensometer. Although the measured results are typically highly accurate, they suffer from a few drawbacks including difficulty in handling and application, unwanted force at the contact area, and limited measuring sites.

Various full-field non-contact methods have been proposed to overcome these drawbacks since the 1950s. Interferometric techniques, including holography interferometry, speckle interferometry, and moire interferometry, emerged with the widely available coherent light source [64]. With the reduced cost and increased resolution/speed of the modern image sensor, the novel non-contact full-field method digital image correlation has attracted

increasing attention in multiple areas including experimental mechanics. It is capable to derive full-field displacement and strain information by comparing the captured digital images of the specimen during deformation. Comparing with the interferometric techniques, DIC does not require the complex optical system and rigorous experimental environment. The specimen preparation for DIC is also simple. Therefore, DIC has been applied in the room temperature tensile test [58], high temperature tensile test [16], nondestructive evaluation [13], fracture test [39, 67], bending test [12], measurement of the coefficient of thermal expansion [11, 51], and many other areas since the invention in 1980s [54].

DIC is essentially an optical tracking method that the adopted algorithm determines the accuracy of the results and efficiency of the matching process. Much effort has been devoted to enhancing the accuracy, robustness, and efficiency of DIC algorithms. Inverse compositional Gauss-Newton algorithm (IC-GN) [46] is the most widely used DIC algorithm in the subpixel level searching stage for its high accuracy and efficiency. Besides, 3D-DIC has been developed to derive the 3D deformation field based on the principle of binocular stereovision [34].

1.2. RESEARCH OBJECTIVES

The main objective of this research is to improve the accuracy and efficiency of DIC method and apply it to the miniature mechanical test. Specifically, the pixel level searching algorithm and reference frame update strategy of DIC are studied first. Then the improved DIC technique is incorporated with the specially designed miniature specimen to derive the constitutive relation beyond necking from the miniature tensile test.

1.2.1. Pixel Level Searching Algorithm. DIC algorithm usually consists of the pixel level searching stage and subpixel level searching stage. The pixel level searching stage provides the initial guess of the displacement vector with the accuracy of a few pixels for the subpixel level searching stage. Then the later improves the accuracy to the level of 0.01 pixel. Forward additive Newton-Raphson algorithm (FA-NR) [5] and

more computational efficient inverse compositional Gauss-Newton algorithm (IC-GN) [46] are most widely used subpixel level searching algorithms. These algorithms are good at accurately finding local deformation parameters. However, an initial guess close to the global optimum need to be provided to these algorithms first. Otherwise, they may fall into local optimum due to the sensitivity of the gradient-based method.

While subpixel level searching methods receive much research attention, there are only a few studies regarding the improvement of the initial guess. Integer-pixel searching (IPS) algorithm is typically employed to generate the initial pixel level displacement. This algorithm calculates cross correlation coefficient of a subset at candidate positions locate around POI. The integer displacement to the location with the highest similarity will be the initial guess. Nevertheless, it is considered to be computationally intensive. Tsai and Lin [66] utilized the precomputed sum-table to increase computational efficiency. Conducting the calculation in the spectral domain could largely increase the speed via fast Fourier transformation (FFT) [31]. Zhao *et al.* [77] and Wu *et al.* [71] utilized population-based method algorithms to accelerate calculation.

Besides the computational burden, one limitation of the IPS method is the assumption of the dominant rigid body translation. In the case of large nonuniform deformation or rotation, the assumption would not hold. Another drawback is that it may generate a few outliers have evident incompatible displacements with other POIs, and these outliers are hard to be removed conveniently. Because the pixel level searching is conducted individually for each POI and no continues deformation constraint is applied. To overcome this weakness, the reliability-guided method [41, 68] was proposed to eliminate the need for pixel level searching except for the seed point.

Finding correct correspondence of the same point between two images is a fundamental problem in computer vision, and it is an essential precondition in many applications including object tracking, pose estimation and 3D reconstruction. The correspondence is usually found at unique points, namely feature points, in images. Information from a

local region around the feature point could be extracted by the feature descriptor. Thus the correspondence of feature points could be detected from the similarity between feature descriptors. The resemblance between feature matching and estimating initial guess in DIC makes it is possible to take advantage of well-developed techniques by the computer vision community. Zhou *et al.* [80] obtained initial deformation parameters for the seed point by matching scale-invariant feature transform (SIFT) features. To eliminate possible false matched pairs, preliminary matches were filtered out by random sampling consensus (RANSAC) algorithm to fit into an affine transformation. Then after subpixel level searching, refined deformation parameters of the seed point is transferred to one of its neighbors through the reliability-guided procedure. A similar approach was applied by Wang *et al.* [70] with improved random sampling consensus (iRANSAC) to cope with the case with large deformation and rotation or images have periodic patterns. Zhou and Chen [79] expanded this approach into 3D-DIC and extracted correct matches by selecting feature points that persevere the number of neighbor features. Nevertheless, these investigations have been focused on getting the initial deformation parameter of a seed point by fitting an affine transformation into the feature points around the seed point. One limitation of the seed point and reliability-guided method is that it is a serial approach and hard to be parallelized. Moreover, the affine transformation assumes the uniform deformation condition that will be only approximately valid in a small region and in the small deformation case.

The objective of this study is to provide an algorithm that robustly estimates initial guesses for POIs in a large region even in the case of large nonuniform deformation or rotation.

1.2.2. Reference Frame Update Strategy. The surface patterns that carry the deformation information may change considerably during the test due to many unavoidable factors. The varied surface pattern makes it extremely difficult if not impossible to directly find the corresponding locations in the last frame from the initial frame, e.g., the decorrelation effect occurs [45]. However, only limited researches have been committed to solving

this problem. One trivial solution would be changing the reference frame at a constant frame step, e.g., the constant step strategy (CS). Nevertheless, the selection of the appropriate step is not a trivial problem. If the step is too large, the decorrelation could still happen. If the step is too small, the small error generated at each reference frame calculation will be accumulated, and the results would not be accurate. Besides, the CS strategy could not account for varying conditions including different loading rate, illumination, noise level, etc.

Pan *et al.* [45] proposed an incremental reliability guided (IRG) technique regarding this problem. The reliability guided method was introduced in [41] that the initial guess for every POI is from the converged deformation parameter of its neighbors with the highest zero normalized cross-correlation coefficient (ZNCC). The initial guess of the first POI, called the seed point, is from integer pixel displacement searching. The IRG strategy determines a new reference frame has to be used only when the ZNCC of the seed point is smaller than a predefined threshold. Tang *et al.* [65] suggested another approach. They utilized the deformation parameter of the seed point in $(n-1)$th frame to initialize the shape of the subset in the reference frame and then match it in the nth frame. This method is quite similar to the template update strategy in visual tracking area [38]. It is equivalent to use the deformation parameter in the $(n-1)$th frame as the initial guess for the nth frame. The reference frame update criterion in [65] is the standard deviation of grayscale residual larger than a predefined value. Another approach called the single step DIC was proposed by Goh *et al.* [15]. The loading force and displacement are used to estimate the deformation parameter and initiate subpixel level searching. They claimed that it does not need to update the reference frame.

Although these methods are more flexible than the CS strategy, each one has its limitation. One obvious drawback of the IRG strategy is that each time only the ZNCC of one or several seed points was examined to determine if the reference frame need be updated. It could not guarantees all other POIs could be successfully matched with this frame step

due to the possible large local deformation. Also, the IRG strategy uses the $(n-1)$th frame as the current frame if the calculated ZNCC of the seed point in the nth frame is below the threshold. This strategy of reducing the frame step may present a performance issue that several consecutive current frames may all fail due to their similar states. In [65], the physical meaning of the criterion of the standard deviation of the grayscale residual is not clear. Single step DIC [15] only works for the elastic deformation situation like the rubber used in the experiment and replies on additional loading data.

The objective of this part of research is to propose a simple but effective strategy to solve the reference frame update problem in multiple situations.

1.2.3. Determination of Constitutive Relation from Miniature Tensile Test. The tensile test is the fundamental and widely used technique to obtain the strength and ductility properties and stress-strain behavior of materials. Therefore, the miniature tensile test is the most widely studied miniature test. However, in contrast to the standard tensile specimen specified in ASTM E8 or ISO 6892, many different designs of miniature tensile specimens have been proposed [7, 17, 18, 26, 27, 28, 55, 78]. They feature different dimensions of the gauge section, aspect ratio of the cross-section, radius of the fillet, and gripping mechanism. One conclusion could be drawn from the results of various miniature tensile tests, the determined yield strength, ultimate strength, and uniform elongation are comparable to the standard specimen results. Chen et al. [7] concluded that the yield strength of the CuAl7 alloy decreased with increasing thickness then stabilized when the thickness was larger than 0.5 mm. The yield strength is nearly constant when the ratio of thickness t to grain size d is larger than a critical value (about 21). This is coincident with [28], in which the critical ratio was 16, 3.4 and 1.5 for 20MnMoNi55, CrMoV and SS304LN, respectively.

Most mentioned miniature tensile research focused on the properties of yield strength, ultimate strength, uniform elongation, and ultimate elongation, the true constitutive relation was seldom considered. Gussev et al. [17] noticed that the true stress-strain

curves describing strain-hardening behavior were very close for different types of specimens. However, these true stress-strain curves were only calculated till the ultimate stress, e.g., the end of uniform deformation. The true constitutive relation at large strain is important in plastic analysis and large deformation simulation. The true stress-strain curve represents the deformation of the yield surface in the stress space. While the engineering stress-strain curve determined from the ordinary uniaxial tensile test is extensively used for characterizing plastic hardening behavior of metals, the result becomes invalid after the maximum load or the onset of necking due to the nonuniform deformation and triaxial stress state. More complicated measurement and analysis need to be applied to get the true constitutive relation at large strain.

In general, two types of approaches have been widely studied to derive the constitutive relation. The first approach is the correction method initially developed by Bridgman [4] in the 1950s. This method relies on the continuous measurement of the area of cross-section and the radius of curvature in the neck of the cylindrical specimen. The true axial stress is first calculated based on the instantaneous area of the cross-section, then it is multiplied by a correction factor to yield the equivalent stress. The analytical correction factor is based on a few assumptions. Later, Le Roy et al. [30] proposed a simplified equation to calculate the correction factor that eliminates the requirement of the radius of curvature. The correction method has been extended to specimens with rectangle cross-section [10, 59, 76]. These analyses were based on FEA simulation since an analytical solution for specimens with rectangle cross-section is hard to get. In order to measure the instantaneous area of the cross-section, interrupted tests were possible but burdensome [10]. To overcome this limitation, the non-contact optical metrology method digital image correlation (DIC) was applied to continuously measure the area of the cross-section without interruption for cylindrical [82] and rectangle [72] specimens. However, complex mirrors or multiple cameras are required for these DIC setups.

Another type of approach is the inverse FEA method, which iteratively adjusts the true stress-strain curve in the FEA simulation to match the experimentally measured quantities such as virtual work [24], load force [21, 32], or axial stress [22]. The advantage of the inverse FEA method is that the description of the true stress-strain curve could be the piece-wise linear function instead of the predefined model. However, the limitation is that the iterative process is laborious and time-consuming.

The objective of the current research is to provide a simple method to determine the constitutive behavior of material up to the onset of localized necking by miniature tensile test and DIC. Only one camera with the telecentric is required in the DIC setup that provides the accurate and continuous measurement of the cross-section area. The correction method is used in this research for its simplicity. Overall, the proposed method is easy to be applied in the real application.

1.3. ORGANIZATION OF THE DISSERTATION

The background of this research was first presented in the previous section, where a survey of existing research on miniature mechanical test and optical metrology method was given. Based on the background, the main research objectives were proposed. Three research papers addressing the objectives were included in this thesis.

The first paper proposed a new feature-matching based pixel-level searching algorithm. Oriented FAST and Rotated BRIEF features are semi-uniformly extracted from the region of interest and matched to provide initial deformation information. False matched pairs are eliminated by the novel feature guided Gaussian mixture model point set registration algorithm, and nonuniform deformation parameters of the versatile reproducing kernel Hilbert space function are calculated simultaneously. Validations on simulated images and real-world mini tensile test verify that this scheme can robustly and accurately compute initial guesses with semi-subpixel level accuracy in cases with small or large translation, deformation, or rotation.

In the second paper, a simple but effective bisection searching (BS) strategy is presented to automatically update the reference frames in the DIC analysis. The key idea of this strategy is that the frame step reduces into one half for the unconverged locations and the intermediate frame is utilized to assist the correlating process. This process is iteratively conducted to adjust the frame step in different stages automatically. The performance of the BS strategy is evaluated against the constant step (CS) update strategy on simulated experiments. The results indicate that the BS strategy can automatically adjust the frame step for changing speckle pattern and loading rate. The accuracy and robustness of the BS strategy are better than the CS strategy with the same pixel level and subpixel level searching algorithms. The BS strategy also successfully tracked all POIs and adjusted the frame step in the real world experiment with changing loading rate and large plastic deformation (over 70% engineering strain).

The third paper focused on the application of the DIC method in the miniature tensile test. A convenient experimental method to determine the true stress-strain curve from the miniature tensile test is proposed. The instantaneous cross-section area is estimated by only one camera in aid of DIC technique. This method is applied to a commercial pure Titanium (CP Ti) and Aluminum 6061 alloy (Al6061) for both miniature and standard size specimens. The results show that the extracted true stress-strain curves are highly matched for different dimensions. The correctness of the true stress-strain curve was evaluated by the finite element analysis (FEA) method. Finally, the constitutive behavior of additively manufactured and wrought stainless steel 304L (SS304) was also determined by the proposed method.

PAPER

I. IMPROVED INITIAL GUESS WITH SEMI-SUBPIXEL LEVEL ACCURACY IN DIGITAL IMAGE CORRELATION BY FEATURE BASED METHOD

Yunlu Zhang

Department of Mechanical & Aerospace Engineering

Missouri University of Science and Technology

Rolla, Missouri 65409–0050

Email: yzdyf@mst.edu

ABSTRACT

The quality initial guess of deformation parameters in digital image correlation (DIC) has a serious impact on convergence, robustness, and efficiency of the following subpixel level searching stage. In this work, an improved feature-based initial guess (FB-IG) scheme is presented to provide initial guess for points of interest (POIs) inside a large region. Oriented FAST and Rotated BRIEF (ORB) features are semi-uniformly extracted from the region of interest (ROI) and matched to provide initial deformation information. False matched pairs are eliminated by the novel feature guided Gaussian mixture model (FG-GMM) point set registration algorithm, and nonuniform deformation parameters of the versatile reproducing kernel Hilbert space (RKHS) function are calculated simultaneously. Validations on simulated images and real-world mini tensile test verify that this scheme can robustly and accurately compute initial guesses with semi-subpixel level accuracy in cases with small or large translation, deformation, or rotation.

Keywords: digital image correlation, feature matching, image matching, Gaussian mixture model, initial guess

1. INTRODUCTION

Digital image correlation (DIC) is an optical deformation measurement method. Primary advantages of DIC include simple implementation, low environment requirements, and non-contact full-field measurement [19]. Therefore, DIC has been applied in the room temperature tensile test [27], high temperature tensile test [8], nondestructive evaluation [7], fracture test [14, 31], bending test [6], measurement of the coefficient of thermal expansion [5, 21], and many other areas since the invention in 1980s [24]. Besides applications, much effort has also been devoted to enhancing accuracy, robustness, and efficiency of DIC algorithms.

DIC algorithm usually consists the initial pixel level and subpixel level searching stage. The subpixel level searching stage commonly falls into two categories: subset-based (local) DIC and fullfield-based (global) DIC. The fundamental difference between these two categories is that the calculation of a point of interest (POI) is independent from other POIs in local DIC or should follow displacement continuity constraint in global DIC. Forward additive Newton-Raphson algorithm (FA-NR) [3] and more computational efficient inverse compositional Gauss-Newton algorithm (IC-GN) [18] are most widely used subpixel level searching algorithms. These algorithms are great at finding local optimal deformation parameters accurately. However, an initial guess close to the global optimum need to be provided to these algorithms first. Otherwise, they may fall into local optimum due to sensitivity of the initial value. Besides, an initial guess for full-field DIC [13, 20, 29] is also essential and is beneficial for convergence if it is close to the global optimum.

While subpixel level searching methods receive much research attention, there are only a few studies regarding the improvement of the initial guess. Integer-pixel searching (IPS) algorithm is typically employed to get initial pixel level displacement. This algorithm

calculates cross correlation coefficient of a subset at candidate positions locate around POI. The integer displacement to the location with highest similarity will be the initial guess. Nevertheless, it is considered to be computation intensive. Tsai and Lin [30] utilized the precomputed sum-table to increase computational efficiency. Conducting the calculation in the spectral domain could largely increase the speed via fast Fourier transformation (FFT) [10]. Zhao *et al.* [35] and Wu *et al.* [34] utilized population-based method algorithms to accelerate calculation. Besides the computational burden, one limitation of the IPS method is that it assumes the dominant rigid body translation. In the case of large nonuniform deformation or rotation, the assumption would not hold true. Another drawback is that it may generate a few outliers have evident incompatible displacements with other POIs and are hard to be removed conveniently. Because the pixel level searching is conducted individually for each POI and no continues deformation constrain is applied. To overcome this weakness, the reliability-guided method [16, 32] was proposed to eliminate the need for pixel level searching except the seed point.

Finding correct correspondence between two images is a fundamental problem in computer vision and it is an essential precondition in many applications including object tracking, pose estimation, and 3D reconstruction. The correspondence is usually formed via unique points, namely feature points, in images. Information from a local region around the feature point could be extracted by the feature descriptor. Thus the correspondence of feature points could be detected from similarity between feature descriptors. Resemblance between feature matching and estimating initial guess in DIC makes it is possible to take advantage of well-developed techniques by computer vision community. Zhou *et al.* [37] obtained initial deformation parameters for the seed point by matching scale-invariant feature transform (SIFT) features. To eliminate possible false matched pairs, preliminary matches were filtered out by random sampling consensus (RANSAC) algorithm to fit into an affine transformation. Then after subpixel level searching, refined deformation parameters of the seed point is transferred to one of its neighbors through reliability-guided procedure.

A similar approach was applied by Wang *et al.* [33] with improved random sampling consensus (iRANSAC) to cope the case with large deformation and rotation or images have periodic patterns. Zhou and Chen [36] expanded this approach into 3D-DIC and extracted correct matches by selecting feature points that persevere the number of neighbor features. Nevertheless, these investigations have been focused on getting the initial deformation parameter of a seed point by fitting an affine transformation into the feature points around the seed point. One limitation of the seed point and reliability-guided method is that it is a serial approach and hard to be parallelized. Moreover, the affine transformation assumes the uniform deformation condition that will be only approximately valid in a small region and in the small deformation case.

In the present research, we propose a novel feature-based initial guess (FG-IG) scheme to robustly estimate initial guesses for POIs in a large region even in the case of large nonuniform deformation or rotation. The feature matching part of the scheme is based on newly developed feature guided Gaussian mixture model (FG-GMM) [12]. The proposed method is capable of calculating all six deformation parameters with semi-subpixel level accuracy directly from reproducing kernel Hilbert space (RKHS) coefficients. The rest of the paper is organized as follow. The feature-based scheme is detailed in Section 2. The FB-IG and IPS method are validated against simulated images and real world tensile tests in Section 3. Finally, conclusions are given in Section 7.

2. INITIAL GUESS OF DEFORMATION PARAMETERS BY FEATURE-BASED METHOD

2.1. BASIC PRINCIPAL OF DIGITAL IMAGE CORRELATION

The goal of the DIC algorithm is to obtain displacements and strain field within the region of interest (ROI) from the video or images of the specimen in different states. For subset-based DIC, it is archived by tracking POIs, e.g. centers of subsets. Positions of POIs

are known in the reference image and needed to find out deformed positions in the current image. The reference and current image usually are the undeformed and deformed image respectively. The reference image can also be the deformed image that positions of POIs have been determined previously in the incremental scheme [17].

A subset is typically a small square image patch around POI. The deformation field inside this subset is commonly approximated by the first order shape function. Coordinates of any point in the deformed subset in the current image are

$$\begin{aligned} x^* &= x + u + u_x(x - x_0) + u_y(y - y_0) \\ y^* &= y + v + v_x(x - x_0) + v_y(y - y_0) \end{aligned} \tag{1}$$

where (x, y) is coordinates of corresponding point in the undeformed subset, (x_0, y_0) is coordinates of POI in the reference image. u and v are the displacements in x and y directions, u_x, u_y, v_x, v_y are first order gradients. The combination of $[u, v, u_x, u_y, v_x, v_y]$ is called the deformation parameter $\boldsymbol{p}$.

The objective of subset based DIC is to find the best deformation parameter $\boldsymbol{p}$ that maximizes similarity of subsets matrices in both images. There are various criteria available to quantify similarity of matrices and Pan *et al.* [22] proved that most of them are equivalent. Zero-mean normalized cross correlation (ZNCC) criterion is adopted here for its invariance to linear illumination change.

The ZNCC coefficient of two subsets in the reference and current image is

$$C_{ZNCC}(\boldsymbol{p}) = \frac{\sum_\Omega (F(x, y) - \bar{F})(G(x^*, y^*) - \bar{G})}{\sqrt{\sum_\Omega (F(x, y) - \bar{F})^2} \sqrt{\sum_\Omega (G(x^*, y^*) - \bar{G})^2}} \tag{2}$$

where $F(x, y)$ and $G(x^*, y^*)$ are intensity values in the reference and current images, $\bar{F}$ and $\bar{G}$ are mean intensity values of the subsets, Ω is the set of points in the subset. The possible range of C_{ZNCC} is $[-1, 1]$. The higher the value of C_{ZNCC} represents higher similarity

between two matrices. C_{ZNCC} represents the exact match. For deformed positions (x^*, y^*) not on integer pixels, e.g. subpixel positions, an interpolation scheme should be employed. Bi-cubic b-spline interpolation is used in this research.

As mentioned previously, FA-NR and IC-GN are effective algorithms to solve the nonlinear multi-variable optimization problem. The more computational efficient IC-GN algorithm is adopted in this research. However, these gradient-based methods only converge to the global optimum when a close initial guess is provided. The IPS method is commonly selected as the pixel level searching algorithm. The idea of this algorithm is simply compare C_{ZNCC} of subsets centers around POI in the current image. The location with highest C_{ZNCC} is considered the initial position for subpixel level searching.

2.2. FEATURE EXTRACTOR AND PROMOTING UNIFORMLY DISTRIBUTED FEATURES

Features are interest and unique locations in images that can be easily compared and tracked. By extracting feature in the reference and current image and correctly matching corresponding pairs, the deformation field on these specific locations is obtained. This is the fundamental idea of estimation the initial guess by the feature-based method.

SIFT [11] and speeded up robust features (SURF) [2] are two widely used feature extractors in computer vision. However, these gradient-based descriptors impose a computational burden in the application. Oriented FAST and Rotated BRIEF (ORB) [26] were proposed to enhance the speed while without loss robustness. Main contributions include an oriented FAST (features from accelerated segment test) feature detector [25] and an oriented BRIEF (binary robust independent elementary features) feature descriptor [4]. Therefore, ORB descriptor is adopted in this research.

One problem associated with ORB and most feature detectors is the lack of consideration of the spatial distribution of detected features. The only criterion to select a candidate feature point is its cornerness response. This nonuniform character degrades the matching quality when only a few features are extracted in a part of the interested region while unnecessary dense features in certain regions may waste computation power.

An effort [28] was made to modify the standard SIFT detector to generate more uniformly distributed features. In principle, the same approach could be utilized in the FAST detector. However, a simpler yet effective clustering method is proposed that no alteration of the feature detector algorithm itself is required. Figure POIs are shown in Figure 1(a) that cover the surface of the specimen in the bottom. Features inside a patch of the image that encompass all POIs with additional padding length are detected to limit detected features inside ROI or close to its boundary and save computation time as shown in Figure 1(c). With the clustering approach, all POIs are clustered into groups of points in the reference image by the k-means clustering method as shown in Figure 1(b). A small patch of the image encompasses each cluster with additional padding length is detected for features separately. All of detected feature points from each patch are combined. Some redundant feature points may appear due to the overlap regions of patches. They are removed before proceeds. Detected features with the clustering method appear to be more uniformly distributed in Figure 1(d) than the original approach. It should be noted that the number of detected features by the clustering method is less than the original approach due to removal of redundant points. However, unnecessarily dense feature points are gathered on the left side of Figure 1(b) that do not provide effective information.

Detected features are fed into the FB-IG method as detailed in the next subsection and followed by subpixel level searching. C_{ZNCC} after subpixel level searching proves the influence of the quality of initial guess shown in Figure 1(e, f). There are fewer feature points in the lower right region in the original approach. Consequently, they provide less accurate initial guess and lead less accurate calculated C_{ZNCC}. In contrast, the result of

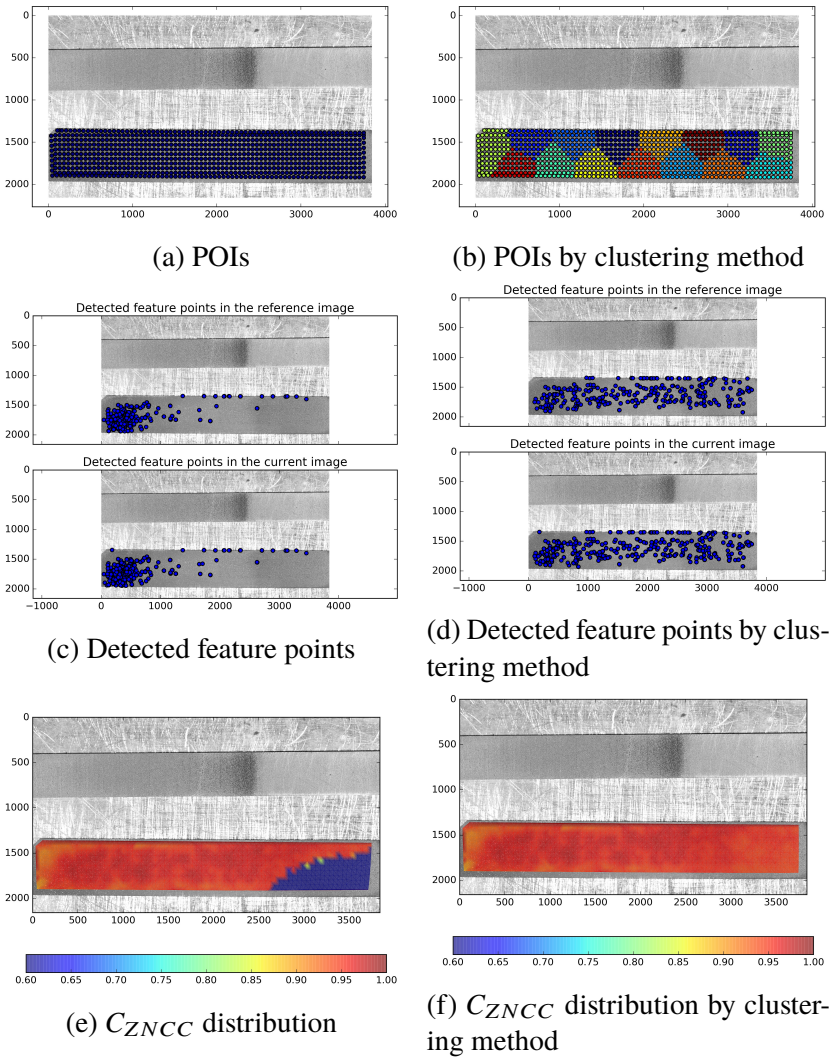

(a) POIs

(b) POIs by clustering method

(c) Detected feature points

(d) Detected feature points by clustering method

(e) C_{ZNCC} distribution

(f) C_{ZNCC} distribution by clustering method

Figure 1. Comparison detected feature points and calculated C_{ZNCC} without (a, c, e) and with (b, d, f) the clustering method. (a) unclustered and (b) clustered POIs. (c) and (d) Detected feature points in the reference and current image. (e) and (f) distribution of calculated C_{ZNCC} after subpixel level searching based on different initial feature points.

the clustering approach shows more uniformly distributed feature points and higher C_{ZNCC} across ROI. The average and standard deviation of C_{ZNCC} by the clustering method are 0.958 and 0.016 respectively that show the high quality of correlation.

2.3. FEATURE GUIDED GAUSSIAN MIXTURE MODEL

Extracted features in the reference and current image are initially matched according to Hamming distance of binary descriptors. To accurately construct the deformation field from initial matched feature pairs, there are two crucial problems need to be addressed. First, a versatile deformation function should be adopted to describe the possible large nonuniform deformation or rotation on the region encompass all feature points. The affine transformation utilized in [36, 37] to model the local deformation around a seed point is not capable. Second, initial matched pairs may contain a certain number of false pairs due to similar patterns in the image that need to be excluded.

FG-GMM [12] is a recently proposed algorithm to compute feature points correspondence and the spatial transformation simultaneously. Main improvements include formulation optimization process into a Gaussian mixture model (GMM), aid the point set registration problem with local feature information, and modeling the spatial transformation via the RKHS function [1]. Key points of FG-GMM with minor modifications for DIC are presented next.

Suppose the number of extracted feature points in the reference and current image are N and M respectively. $\boldsymbol{X}$ and $\boldsymbol{Y}$ are arrays store coordinates of feature points with size $N \times 2$ and $M \times 2$. N feature points in the reference image have corresponding N feature points in the current image by binary descriptor matching. The matching is cross checked to ensure the feature point of each pair is closest among all candidates. Due to nature of local features matching, the result may contain some false matched pairs. In general, matched pairs with large displacement (e.g., 1/10th of the dimension of the image) can be easily determined to be false pairs. Nevertheless, the remaining pairs may still not all be correct.

The objective of this algorithm is to maximize the probability of presence of feature points in the current image $\boldsymbol{Y}$ with the GMM. Centroids of Gaussian densities are deformed feature points $\mathcal{T}(\boldsymbol{X})$ from the reference image. Any point $\boldsymbol{y}_m$ in $\boldsymbol{Y}$ may come from two sources: a random outlier or transformed feature points $\mathcal{T}(\boldsymbol{X})$. A popular assumption is

equal isotropic covariances $\sigma^2\mathbf{I}$ on all GMM components and uniform distribution $1/a$ for outliers [15]. a is the area of the bounding box of $\boldsymbol{Y}$. The set of unknown parameters is $\boldsymbol{\theta} = \{\mathcal{T}, \sigma^2, \gamma\}$, where $\gamma \in [0, 1]$ is the probability of outliers. Thus the probability of a feature point in the current image $\boldsymbol{y}_m$ is

$$\begin{aligned} p(\boldsymbol{y}_m|\boldsymbol{\theta}) &= \gamma\frac{1}{a} + (1-\gamma)\sum_{n=1}^{N}\pi_{mn}\mathcal{N}(\boldsymbol{y}_m|\mathcal{T}, \sigma^2, \gamma) \\ &= \gamma\frac{1}{a} + (1-\gamma)\sum_{n=1}^{N}\frac{\pi_{mn}}{2\pi\sigma^2}e^{-\frac{\|\boldsymbol{y}_m - \mathcal{T}(\boldsymbol{x}_n)\|^2}{2\sigma^2}} \end{aligned} \tag{3}$$

where π_{mn} is the membership probability of GMM. More specifically, π_{mn} represents the probability of a feature point y_m corresponds the deformed feature point x_n. Traditionally, π_{mn} is set to be equal for all GMM components, i.e., $\pi_{mn} = 1/N, \forall m \in \mathbb{N}_M, \forall n \in \mathbb{N}_N$ [9, 15]. To utilize the information from local feature matching, π_{mn} is set to be τ if the feature point in the current image $\boldsymbol{y}_m$ matches the feature point $\boldsymbol{x}_n$ in the reference image. For the rest points $\boldsymbol{x}_i, i \neq n$, π_{mn} is set to be $(1-\tau)/(N-1)$. Here τ is the confidence of feature correspondence. If there is not a feature point in $\boldsymbol{X}$ corresponds the feature point $\boldsymbol{y}_m$, π_{mn} is set to be $1/N$. Therefore, π_{mn} satisfies the constraint $\forall m, \sum_{n=1}^{N}\pi_{mn} = 1$. In this way, the membership probability π_{mn} is "softly" assigned to all $\boldsymbol{y}_m$ while considering information of matched feature pairs.

Then, the goal of FG-GMM is to maximize the log-likehood function

$$\mathcal{L}(\boldsymbol{\theta}|\boldsymbol{Y}) = \sum_{m=1}^{M}\ln p(\boldsymbol{y}_m|\boldsymbol{\theta}). \tag{4}$$

The two interconnected problems mentioned previously becomes finding the optimized parameter set $\boldsymbol{\theta}$ and correspondence probability p_{mn}, which can be defined as the posterior probability $p_{mn} = p(\boldsymbol{y}_m \text{ matches } \boldsymbol{x}_n|\boldsymbol{y}_m) = \pi_{mn}p(\boldsymbol{y}_m|\boldsymbol{y}_m \text{ matches } \boldsymbol{x}_n)/p(\boldsymbol{y}_m)$. Roughly

speaking, the difference between π_{mn} and p_{mn} is that π_{mn} is only from the local feature matching information while p_{mn} also considers the spatial distribution of transformed feature points $\mathcal{T}(\boldsymbol{X})$.

A common solution for the interconnected optimization problem is expectation and maximization (EM) algorithm. It alternates between the expectation step (E-step) and the maximization step (M-step). The E-step aims to estimate the correspondence probability p_{mn} by using the previous calculated parameters $\boldsymbol{\theta}^{\text{old}}$. The M-step finds the new parameters $\boldsymbol{\theta}^{\text{new}} = \arg\max \mathcal{L}(\boldsymbol{\theta}|\boldsymbol{Y})$.

In the E-step, first, the posterior probability p_{mn} of unmatched feature points in the current image are computed by Bayes' theorem:

$$p_{mn} = \frac{\pi_{mn} e^{-\frac{\|\boldsymbol{y}_m - \mathcal{T}(\boldsymbol{x}_n)\|^2}{2\sigma^2}}}{\sum_{k=1}^{N} \pi_{mk} e^{-\frac{\|\boldsymbol{y}_m - \mathcal{T}(\boldsymbol{x}_k)\|^2}{2\sigma^2}} + \frac{2\gamma\pi\sigma^2}{(1-\gamma)a}}. \tag{5}$$

Second, the list of matched and unmatched feature points in the current image will be updated according to the new posterior probability p_{mn}. Feature point $\boldsymbol{y}_m$ is considered to be matched with $\boldsymbol{x}_n$ if $p_{mn} > \eta$ where $\eta \in [0, 1]$ is a predefined threshold. Otherwise, it is unmatched. The membership probability of matched feature points are then updated to τ or $(1 - \tau)/(N - 1)$ for corresponding $\boldsymbol{x}_n$ or the rest feature points. In this way, the initial false matched pair can be corrected as the iterative computation proceeds. Third, the posterior probability p_{mn} of matched feature points are calculated according to Eq. 5 with updated π_{mn}. It should be noted that in the current implementation the list of matched and unmatched pairs are updated in every iteration while in [12] it is only calculated after convergence.

In the M-step, the optimization problem of $\mathcal{T}$ is solved first. After derivation [12], the problem becomes minimizing the energy function

$$\mathcal{E}(\mathcal{T}) = \frac{1}{\sigma^2} \sum_{m=1}^{M} \sum_{n=1}^{N} p_{mn} \|\boldsymbol{y}_m - \mathcal{T}(\boldsymbol{x}_n)\|^2 + \lambda\phi(\mathcal{T}) \tag{6}$$

where λ is the parameter to control smoothness of the deformation field $\mathcal{T}$, $\phi(\mathcal{T})$ is the smoothness function that can be defined as the square norm in RKHS, i.e., $\phi(\mathcal{T}) = \phi(f) = \|f\|^2_{\mathcal{H}}$. Here f is the displacement function $f(\boldsymbol{X}) = \mathcal{T}(\boldsymbol{X}) - \boldsymbol{X}$. The Hilbert space $\mathcal{H}$ is defined on the Gaussian kernel $\boldsymbol{\Gamma}(\boldsymbol{x}_i, \boldsymbol{x}_j) = e^{-\beta\|\boldsymbol{x}_i - \boldsymbol{x}_j\|^2} \cdot \mathbf{I}$. Another theorem from [12] is that the optimal solution of Eq. 6 is given by

$$\mathcal{T}(\boldsymbol{X}) = \boldsymbol{X} + f(\boldsymbol{X}) = \boldsymbol{X} + \boldsymbol{\Gamma}(\boldsymbol{X}, \boldsymbol{X}) \cdot \boldsymbol{C} \tag{7}$$

where the element in the Gram matrix $\boldsymbol{\Gamma}(\boldsymbol{X}, \boldsymbol{X})$ is $\Gamma_{ij} = e^{-\beta\|\boldsymbol{x}_i - \boldsymbol{x}_j\|^2}$, the coefficient array $\boldsymbol{C}$ with size $N \times 2$ is determined by

$$(d(\boldsymbol{P}^{\mathrm{T}}\mathbf{1})\boldsymbol{\Gamma} + 2\lambda\sigma^2\mathbf{I})\boldsymbol{C} = \boldsymbol{P}^{\mathrm{T}}\boldsymbol{Y} - d(\boldsymbol{P}^{\mathrm{T}}\mathbf{1})\boldsymbol{X} \tag{8}$$

where the element in posterior probability matrix $\boldsymbol{P}$ is p_{mn}, $d(\cdot)$ is the diagonal matrix, $\mathbf{1}$ is a size M column vector of all ones.

Parameter γ and σ^2 are updated by

$$\gamma = 1 - M_P/M \tag{9}$$

$$\sigma^2 = \frac{\sum_{m=1}^{M}\sum_{n=1}^{N} p_{mn}\|\boldsymbol{y}_m - \mathcal{T}(\boldsymbol{x}_n)\|^2}{2M_P} \tag{10}$$

where $M_P = \sum_{m=1}^{M}\sum_{n=1}^{N} p_{mn}$

E-step and M-step alternatively proceed until either one of two converging conditions is satisfied.

$$\mathcal{L}(\boldsymbol{\theta}^{\mathrm{new}}|\boldsymbol{Y}) \leq \mathcal{L}(\boldsymbol{\theta}^{\mathrm{old}}|\boldsymbol{Y}) + 0.1 \tag{11}$$

$$\|\boldsymbol{C}^{\mathrm{new}} - \boldsymbol{C}^{\mathrm{old}}\| \leq 0.001 \cdot \|\boldsymbol{C}^{\mathrm{old}}\|. \tag{12}$$

The calculation will stop either the increment of the likehood probability $\mathcal{L}(\boldsymbol{\theta}|\boldsymbol{Y})$ is minimal or the change of the norm of coefficient array $\boldsymbol{C}$ is minimal.

2.4. ESTIMATION OF INITIAL DEFORMATION PARAMETERS

The conventional pixel level searching method only yields two integral displacements u and v for the seed point or all POIs. In most DIC research, first order deformation approximation is adopted that utilizes six deformation parameters u, v, u_x, u_y, v_x, v_y. Providing initial guess for all of 6 parameters would be ideal. Now it is achievable based on the deformation field is described by the RKHS function.

Suppose coordinates of POIs in the reference image are stored in a $L \times 2$ array $\boldsymbol{Z}$. Deformed POIs under the deformation field calculated on feature points is

$$\mathcal{T}(\boldsymbol{Z}) = \boldsymbol{Z} + f(\boldsymbol{Z}) = \boldsymbol{Z} + \boldsymbol{\Gamma}(\boldsymbol{Z}, \boldsymbol{X}) \cdot \boldsymbol{C} \tag{13}$$

The displacement is

$$\mathcal{T}(\boldsymbol{Z}) - \boldsymbol{Z} = \boldsymbol{\Gamma}(\boldsymbol{Z}, \boldsymbol{X}) \cdot \boldsymbol{C} \tag{14}$$

where the result is a $L \times 2$ matrix. The first and second column of this matrix are displacements $\boldsymbol{u}$ and $\boldsymbol{v}$ of POIs respectively.

The derivatives of displacements are

$$\frac{\mathrm{d}\mathcal{T}(\boldsymbol{Z})}{\mathrm{d}x} = \frac{\mathrm{d}\boldsymbol{\Gamma}(\boldsymbol{Z}, \boldsymbol{X})}{\mathrm{d}x} \cdot \boldsymbol{C} \tag{15}$$

$$\frac{\mathrm{d}\mathcal{T}(\boldsymbol{Z})}{\mathrm{d}y} = \frac{\mathrm{d}\boldsymbol{\Gamma}(\boldsymbol{Z}, \boldsymbol{X})}{\mathrm{d}y} \cdot \boldsymbol{C}. \tag{16}$$

With the definition of Gaussian kernel, each element of the derivative of the Gram matrix with size $L \times N$ is

$$\left(\frac{\mathrm{d}\boldsymbol{\Gamma}(\boldsymbol{Z}, \boldsymbol{X})}{\mathrm{d}x}\right)_{ij} = -2\beta \left(\Gamma(\boldsymbol{Z}, \boldsymbol{X})\right)_{ij} (Z_{i0} - X_{j0}) \tag{17}$$

$$\left(\frac{\mathrm{d}\Gamma(\boldsymbol{Z}, \boldsymbol{X})}{\mathrm{d}y}\right)_{ij} = -2\beta \left(\Gamma(\boldsymbol{Z}, \boldsymbol{X})\right)_{ij} (Z_{i1} - X_{j1}) \tag{18}$$

where $i \in \mathbb{N}_N$, $j \in \{0, 1\}$. The results of Eq. (15) and (16) are two $L \times 2$ matrices. The first columns of them are $\boldsymbol{u}_x$ and $\boldsymbol{u}_y$, and the second columns are $\boldsymbol{v}_x$ and $\boldsymbol{v}_y$. The deformation parameter array $\boldsymbol{P}$ of size $L \times 6$ is a combination of $[\boldsymbol{u}, \boldsymbol{v}, \boldsymbol{u}_x, \boldsymbol{u}_y, \boldsymbol{v}_x, \boldsymbol{v}_y]$.

2.5. IMPLEMENTATION DETAILS

In computer vision, input data is commonly normalized before performing point set registration. This good practice is adopted here to ensure the result is consistent. More specifically, feature points array $\boldsymbol{X}$ and $\boldsymbol{Y}$ are linearly rescaled to have zero mean and unit variance. For instance, the element of normalized $\boldsymbol{X}$ is

$$X'_{ij} = \frac{X_{ij} - X^c_j}{X^s} \quad i \in \mathbb{N}_N, j \in \{0, 1\} \tag{19}$$

where $\boldsymbol{X}^c$ is the centroid of feature points in the reference image, X^s is the scale parameter, i.e., the standard deviation of $\boldsymbol{X}$. All the calculation detailed in Section 2.3 are performed after normalization. Therefore, the calculated deformed POIs coordinates $\mathcal{T}(\boldsymbol{Z})$ in Eq. (13) are normalized. The derived displacements and gradients on POIs should be denormalized accordingly. Deformed POIs $\boldsymbol{Z}$ are normalized by the centroid and scale of $\boldsymbol{X}$ then denormalized by the centroid and scale of $\boldsymbol{Y}$ after transformation.

$$\boldsymbol{Z}'_{\cdot j} = \frac{\boldsymbol{Z}_{\cdot j} - X^c_j}{X^s} \tag{20}$$

$$\mathcal{T}(\boldsymbol{Z})_{\cdot j} = \mathcal{T}(\boldsymbol{Z}')_{\cdot j} \cdot Y^s + Y^c_j. \tag{21}$$

Considering the normalization-denormalization process, Eq. (15) and (16) become

$$\boldsymbol{u}_x = \frac{\mathrm{d}\mathcal{T}(\boldsymbol{Z}')_{\cdot 0}}{\mathrm{d}x} = \frac{Y^s - X^s}{X^s} + \frac{Y^s}{X^s}\frac{\mathrm{d}\boldsymbol{\Gamma}(\boldsymbol{Z}', \boldsymbol{X}')}{\mathrm{d}x} \cdot \boldsymbol{C}_{\cdot 0} \tag{22}$$

$$\boldsymbol{v}_x = \frac{\mathrm{d}\mathcal{T}(\boldsymbol{Z}')_{\cdot 1}}{\mathrm{d}x} = \frac{Y^s}{X^s}\frac{\mathrm{d}\boldsymbol{\Gamma}(\boldsymbol{Z}', \boldsymbol{X}')}{\mathrm{d}x} \cdot \boldsymbol{C}_{\cdot 1} \tag{23}$$

$$\boldsymbol{u}_y = \frac{\mathrm{d}\mathcal{T}(\boldsymbol{Z'})_{\cdot 0}}{\mathrm{d}y} = \frac{Y^s}{X^s}\frac{\mathrm{d}\boldsymbol{\Gamma}(\boldsymbol{Z'}, \boldsymbol{X'})}{\mathrm{d}y} \cdot \boldsymbol{C}_{\cdot 0} \tag{24}$$

$$\boldsymbol{v}_y = \frac{\mathrm{d}\mathcal{T}(\boldsymbol{Z'})_{\cdot 1}}{\mathrm{d}y} = \frac{Y^s - X^s}{X^s} + \frac{Y^s}{X^s}\frac{\mathrm{d}\boldsymbol{\Gamma}(\boldsymbol{Z'}, \boldsymbol{X'})}{\mathrm{d}y} \cdot \boldsymbol{C}_{\cdot 1} \tag{25}$$

There are multiple parameters need to be initialized in the scheme: $\gamma, \beta, \lambda, \eta, \tau$, etc. Choosing different values for these parameters may influence robustness and efficiency of the algorithm. The values used in the validation section are summarized here. The initial guess for the outliers percentage $\gamma = 0.3$. The coefficient in the Gram matrix $\beta = 0.1$ that controls the width of interaction between feature points. The parameter in the energy function $\lambda = 8$ that controls smoothness of the deformation field. The threshold $\eta = 0.9$ to determine if a match pair is valid. The confidence of matched pairs $\tau = 0.7$. The number of feature points M to be extracted in the current image is set via a parameter called feature area A_f. $M = \mathrm{int}(A_b/A_f)$, where A_b is the area of the bounding box of POIs $\boldsymbol{Z}$ in the reference image. A_f is set to be $700\,\mathrm{px}^2$. The initial number of extracted feature points in the reference image is set to $1.5M$ to provide more candidates feature points to match feature points in the current image. After binary descriptor matching, only matched and pre-filtered feature points in the reference image are kept and the number is N. The number of clusters to divide the POIs is 10. The padding length added to the bounding box of each cluster is 70 px. The initial value of coefficient array $\boldsymbol{C}$ is set to be zero array $\boldsymbol{0}$. The initial value of the posterior probability p_{mn} is set to be identical with π_{mn}. The area a of bounding box of feature points in the current image is calculated after the normalization process.

3. EXPERIMENTAL RESULTS

To test accuracy and robustness of the FB-IG scheme, it was compared with the IPS method against simulated images and real-world tensile tests. The implemented code was written in Python programming language and based on several scientific computational packages including scipy (solving batched linear systems), ArrayFire (GPU accelerated

interpolation), OpenCV (ORB feature detection and matching), and scikit-learn (clustering algorithm). The video acquisition system included a consumer-level camera Panasonic® GX85 and a macro lens Olympus® 60mm/2.8. The resolution of the video was 3840×2160 px and the frame rate was 30Hz.

To compare the performance of the IPS and FB-IG method, initial guesses from both methods were fed into the same IC-GN algorithm to derived subpixel level results. The maximum pixel level searching distance was 8 pixel in consideration of computational efficiency and GPU memory size limitation. If this searching distance limitation was removed, there would be a considerable amount of false initial guesses, especially in the case with periodic surface pattern or large deformation makes the original texture ambiguous. In addition, the sensitivity of the IPS method to rotation may also generate false results if large rotation is presented. Therefore, the limited searching range would not affect the conclusion that the IPS method is not suitable for the case of large deformation.

Three performance indicators were adopted in comparisons: C_{ZNCC} after pixel and sub pixel level searching, change of deformation parameters before and after subpixel level searching stage, and the average number of IC-GN iterations.

3.1. SIMULATED IMAGES VALIDATION

To accurately evaluate and compare the performance of both methods, computer-generated speckle images were used for their precisely control deformation information. The method to generate Gaussian speckles described in [23] was employed to generate the

undeformed image $F(x, y)$ and deformed image $G(x, y)$:

$$F(x, y) = \sum_{k=1}^{s} I_k^0 e^{-((x_k-x)^2+(y_k-y)^2)/R_k^2} \tag{26}$$

$$\begin{aligned} G(x, y) = &\sum_{k=1}^{s} I_k^0 e^{-(x_k+u_k+u_{k,x}(x-x_0)+u_{k,y}(y-y_0)-x)^2/R_k^2} \\ &\cdot e^{-(y_k+v_k+v_{k,x}(x-x_0)+v_{k,y}(y-y_0)-y)^2/R_k^2} \end{aligned} \tag{27}$$

where s is the number of speckle granules, I_k^0, (x_k, y_k), and R_k are the peak intensity, position, and size of each speckle granule respectively. u_k, v_k and $u_{k,x}, u_{k,y}, v_{k,x}, v_{k,y}$ are rigid displacements and gradients of displacement at each speckle granule. (x_0, y_0) is the origin of translation, rotation, and gradient. No additional noise was added in the simulated images.

The size of simulated images was 400×550 px with the 300×450 px speckle region in the center as shown in Figure 2(a). The number of speckle granules s was set to be 8000. The radius and maximum intensity were uniform random distributed in ranges $[1, 7]$px and $[0, 1]$ respectively. The generated images were then linearly rescaled to the range of $[0, 255]$ and converted into integral data type. The gray level distribution of the reference speckle image is indicated in Figure 2(c). The deformation field shown in Figure 2(b) was a combination of translation, rotation, and elongation. The translation is 2 px in the horizontal direction. The rotation is around the center of the left edge by $1/120$ rad counterclockwise. The gradients were set to be $u_{k,x} = 0.015, u_{k,y} = 0, v_{k,x} = 0, v_{k,y} = -0.005$. This complex deformation process resulted that maximum displacements of the speckle granules were 15.9 px and -11.6 px in the horizontal and vertical direction.

Numbers of detected feature points in the reference and current image were 974 and 1386 respectively. Figure 2(b) shows the estimated deformed feature points $\mathcal{T}(\boldsymbol{X})$ in the current image. It can be seen that textures around $\mathcal{T}(\boldsymbol{X})$ match well with undeformed feature points $\boldsymbol{X}$ in the reference image as indicated in Figure 2(a).

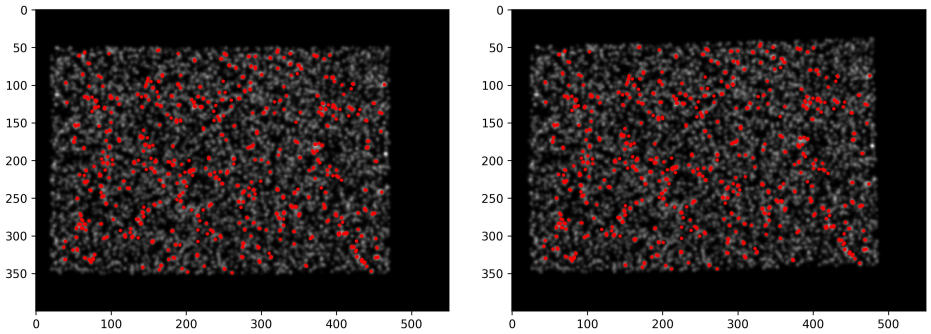

(a) Undeformed image (b) Deformed image

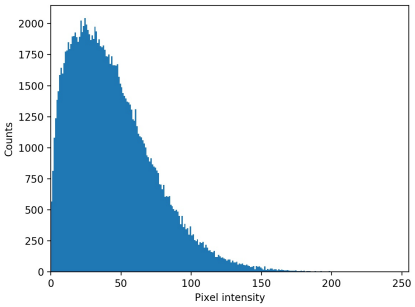

(c) Histogram

Figure 2. Simulated undeformed (a) and deformed (b) images with feature points. (a) Detected feature points $\boldsymbol{X}$ in the reference image. (b) Estimated deformed feature points $\mathcal{T}(\boldsymbol{X})$ in the current image by the FB-IG method. (c) Histogram plot of the reference speckle image.

263 POIs were generated in the reference image as shown in Figure 3(a). Corresponding C_{ZNCC} on these POIs with initial guesses provided by the FB-IG and IPS method are displayed in Figure 3(b, c). C_{ZNCC} calculated from the FB-IG method were uniform and close to 1 that indicates good matching quality. In contrast, C_{ZNCC} on the bottom right region calculated from the IPS method was low and corresponding POIs were distorted. The result confirmed that the IPS method failed to find correct initial guess outside its searching region.

Table 1 summarizes performance indicators of both methods. C_{ZNCC} of the FB-IG method at two stages was both close to 1. The changes of deformation parameters from pixel to subpixel level searching were minimal. On average, it took only 1.4 times of IC-GN

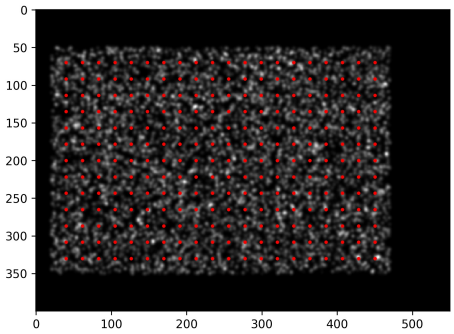

(a) POIs

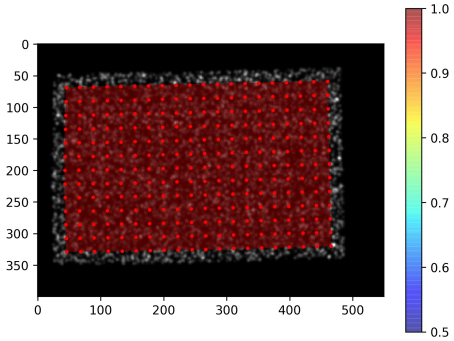

(b) C_{ZNCC} by FB-IG

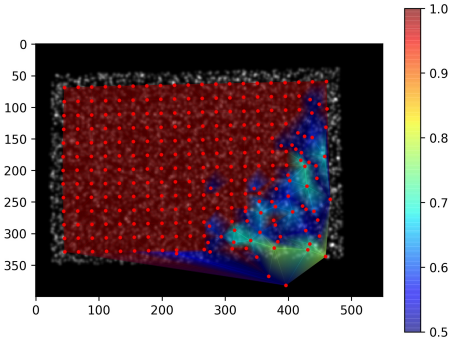

(c) C_{ZNCC} by IPS

Figure 3. Comparison of C_{ZNCC} after subpixel level searching with initial guesses from FB-IG and IPS method in the simulated deformation test. (a) POIs in the reference image. C_{ZNCC} distribution after the pixel level searching stage by (b) FB-IG and (c) IPS methods.

iterations to converge. However, the IPS method generated inferior results on all indicators. One important result was the absolute difference of displacements between calculated and true values. The true values of displacements on POIs were interpolated from the prescribed displacement field of centers of speckle granules. The accuracy of the combination of the FB-IG and IC-GN method proved to be very high with the average difference was only 0.021 ± 0.024 px.

Table 1. Comparison of calculated C_{ZNCC}, deformation parameters changes before and after subpixel level searching stage, and the average number of IC-GN iterations by the FB-IG and IPS method of the simulated deformation test.

	C_{ZNCC} (mean ± std (min))		pixel to subpixel level changes (mean ± std (max))	
	Pixel level	subpixel level	$\boldsymbol{u}, \boldsymbol{v}$ (px)	$\boldsymbol{u}_x, \boldsymbol{u}_y, \boldsymbol{v}_x, \boldsymbol{v}_y$
FB-IG	0.9982 ± 0.0023(0.9846)	0.9996 ± 0.0002(0.9990)	0.062 ± 0.088(0.433)	0.0016 ± 0.0027(0.019)
IPS	0.7790 ± 0.2507(0.2050)	0.8815 ± 0.2444(−0.2153)	1.783 ± 10.149(125.981)	3.57 ± 53.45(863.44)
	Absolute difference of displacements between calculated and true values (mean ± std (max))(px)		Average number of IC-GN iterations	
FB-IG	0.021 ± 0.024(0.113)		1.4	
IPS	3.195 ± 9.144(112.309)		7.1	

3.2. REAL-WORLD TENSILE TESTS

The video of a mini tensile test was used in the real-world validation. The mini copper specimen in the reference image is shown in Figure 4(a). The gauge section was only 3 mm long and corresponds 850 px in the image. The frame step was 400 at first, which corresponded a time step of 13.3 s.

472 and 968 ORB features had been detected and matched around the gauge section by the FB-IG method in the reference and current image as shown in Figure 4(b, c). Deformed feature points $\mathcal{T}(\boldsymbol{X})$ in the current image is shown in Figure 4(d). From visual inspection of the surface texture, feature points $\boldsymbol{X}$ in the reference image match deformed feature points $\mathcal{T}(\boldsymbol{X})$ in the current image. This result indicates that the generated deformation field is correct.

Deformed POIs in the current image with calculated C_{ZNCC} from the FB-IG and IPS method are shown in Figure 5(b, c). It is clear that C_{ZNCC} from FB-IG was uniform and close to 1 and deformed POIs show the same trend of distribution as undeformed POIs in Figure 5(a). The maximum and average displacement of POIs from the FB-IG method were 48.8 px and 25.5 px in the horizontal direction that corresponds 3% average strain. In contrast, only results on the left side from the IPS method were acceptable, C_{ZNCC} of rest POIs was small and POIs were distorted. The reason for this result is that the left side of

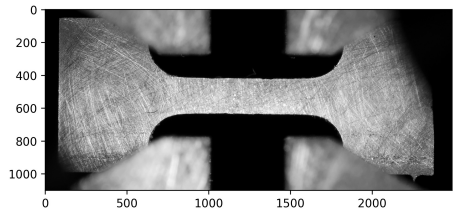

(a) Tensile specimen

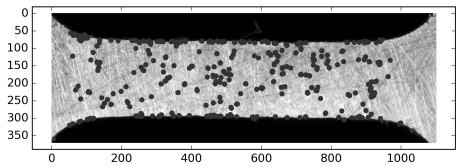

(b) Detected feature points $\boldsymbol{X}$ in reference image

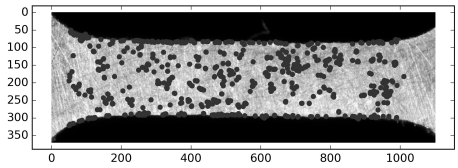

(c) Detected feature points $\boldsymbol{Y}$ in current image

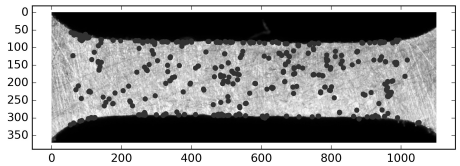

(d) Estimated feature points $\mathcal{T}(\boldsymbol{X})$ in current image

Figure 4. Image of the tensile specimen and detected features. (a) The mini tensile specimen in the reference image. (b) Detected feature points $\boldsymbol{X}$ in the reference image. (c) Detected feature points $\boldsymbol{Y}$ in the current image. (d) Estimated deformed feature points $\mathcal{T}(\boldsymbol{X})$ in the current image by the FB-IG method.

the specimen was fixed and displacements of POIs on the right side were larger than the maximum pixel level searching distance. This phenomenon also agreed with the conclusion that the IPS method only works in the situation of small deformation or rotation.

The frame step was reduced to 60, e.g. time step of 2 s, to test the accuracy of both methods in the small deformation situation. The results shown in Figure 5(d, e) indicate that C_{ZNCC} was all close to 1 and deformed POIs match well with initial ones. The maximum and average displacement of POIs in the horizontal direction were 3.7 px and 7.3 px that were within the integer-pixel searching region.

Table 2 presents C_{ZNCC} before and after subpixel level searching of two methods in the large and small deformation case. Absolute displacements $\boldsymbol{u}, \boldsymbol{v}$ and gradients $\boldsymbol{u}_x, \boldsymbol{u}_y, \boldsymbol{v}_x, \boldsymbol{v}_y$ differences before and after subpixel level searching stage are also listed. The FB-IG method derived larger average C_{ZNCC} and smaller standard deviation of C_{ZNCC} than the IPS method in both cases. In the small deformation case, average C_{ZNCC} maintained the same after IC-GN searching indicated that the initial guess was considerably close to

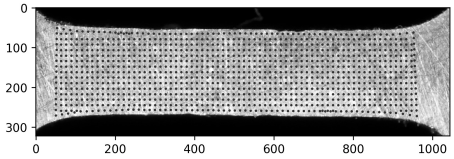

(a) POIs in reference image

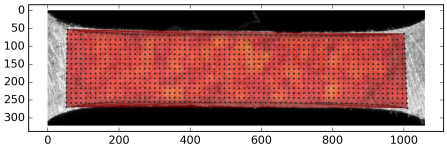

(b) Large deformation by FB-IG

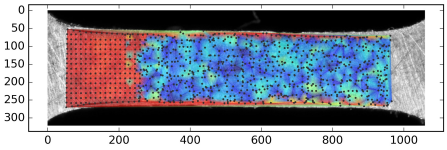

(c) Large deformation by IPS

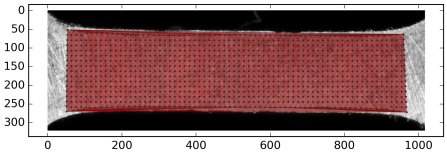

(d) Small deformation by FB-IG

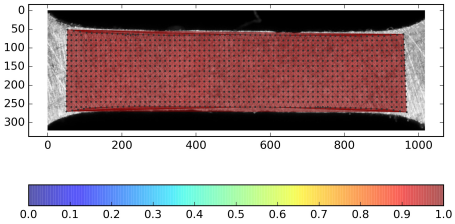

(e) Small deformation by IPS

Figure 5. Comparison of C_{ZNCC} after subpixel level searching with initial guesses from the FB-IG and IPS method in the large and small deformation case of the mini tensile test. (a) POIs in the reference image. C_{ZNCC} distribution by the (b) FB-IG and (c) IPS method in the large deformation case; (d) FB-IG and (e) IPS method in the in the small deformation case.

the global optimum. This result also confirmed with changes of displacements and gradients. The average change of displacements was 0.30 px and 0.14 px in the large and small deformation case respectively. It proved that the initial guess of deformation parameters with semi-subpixel level accuracy was derived from the FB-IG scheme. In the case of small

deformation, the average number of IC-GN iterations from the FB-IG method was less than the IPS method. The result implied that initial guess from the FB-IG method was closer to the final optimum even when both methods provide accurate initial guesses.

Table 2. Comparison of calculated C_{ZNCC}, deformation parameters changes before and after subpixel level searching stage, and the average number of IC-GN iterations by the FB-IG and IPS method in cases of large and small deformation of mini tensile tests.

		C_{ZNCC} (mean ± std (min))		Pixel to subpixel changes (mean ± std (max))		IC-GN
		Pixel level	Subpixel level	$\boldsymbol{u}, \boldsymbol{v}$(px)	$\boldsymbol{u}_x, \boldsymbol{u}_y, \boldsymbol{v}_x, \boldsymbol{v}_y$	Iterations
Large deformation	FB-IG	0.88 ± 0.06(0.49)	0.91 ± 0.04(0.78)	0.30 ± 0.22(1.23)	0.009 ± 0.007(0.040)	4.7
	IPS	0.34 ± 0.32(−0.29)	0.45 ± 0.33(−0.18)	1.19 ± 1.90(28.75)	0.158 ± 0.329(8.471)	20.2
Small deformation	FB-IG	0.98 ± 0.01(0.93)	0.98 ± 0.01(0.96)	0.14 ± 0.12(0.79)	0.003 ± 0.002(0.013)	3.7
	IPS	0.96 ± 0.02(0.84)	0.98 ± 0.01(0.96)	0.26 ± 0.15(0.61)	0.008 ± 0.003(0.017)	4.3

To test robustness of the FB-IG method in the extra large deformation case, the frame step was set to be 800 that corresponded a time step of 26.7 s. The padding length of the bounding box of clusters was set to be 120 px to accommodate the increased maximum displacement. Figure 6 shows calculated feature points and C_{ZNCC}. The maximum and average displacement were 98.1 px and 50.4 px in the horizontal direction, which indicated the maximum elongation was 11.5%. Estimated deformed feature points matched well deformed surface textures as shown in Figure 6(b). The distribution of C_{ZNCC} was still uniform and suggested no obvious de-correlation. The average C_{ZNCC} was 0.798 ± 0.092. The reason of the lower average C_{ZNCC} compared with previous cases may attribute to new surface textures appeared during plastic deformation. C_{ZNCC} could not reach 1 even with the perfect DIC algorithm in this case. Nevertheless, this test proved that the FB-IG scheme was robust in the extra large deformation case.

The computation time of a scheme is related to many factors including the algorithm, image size, frame step, selection of parameters, implementation, and hardware. The average calculation of FB-IG method is $1 \sim 2$ s for 1500 features on a PC, which is on the same level of IPS method for 1000 POIs with vectorized GPU-accelerated code. However, the searching length of the latter method is limited to 8 px.

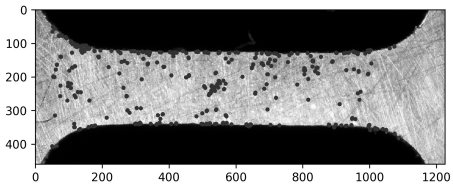

(a) Feature points $\boldsymbol{X}$ in reference image

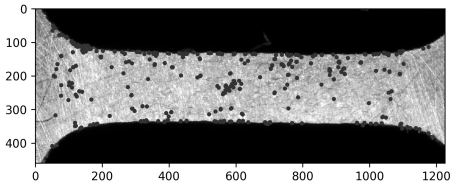

(b) Deformed feature points $\mathcal{T}(\boldsymbol{X})$ in current image

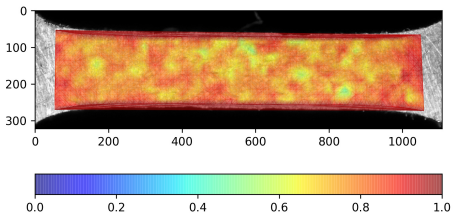

(c) C_{ZNCC} distribution

Figure 6. Feature points and C_{ZNCC} in the extra large deformation case of the mini tensile test. (a) Detected feature points $\boldsymbol{X}$ in the reference image. (b) Estimated deformed feature points $\mathcal{T}(\boldsymbol{X})$ in the current image. (c) C_{ZNCC} after subpixel level searching with initial guesses from the FB-IG method.

4. CONCLUSION

In this paper, the FB-IG scheme is proposed by combining the FG-GMM point set registration algorithm and the ORB feature extractor for pixel level searching in DIC. Extracted features are semi-uniformly distributed in ROI by the clustering method. The global continues deformation field is interpolated on feature points in the reference image by the RKHS function. After solving the optimization problem by the EM algorithm, correct feature pairs and nonuniform deformation field are determined simultaneously. Deformation parameters for all POIs are derived from the deformation field.

ACKNOWLEDGMENT

This project was supported by NASA EPSCoR Grant NNX13AM99A, National Science Foundation Grants CMMI-1547042 and CMMI-1625736, and the Intelligent Systems Center (ISC) and Material Research Center at Missouri S&T. Their financial support is greatly appreciated.

REFERENCES

[1] Aronszajn, N., 'Theory of reproducing kernels,' Transactions of the American mathematical society, 1950, **68**(3), pp. 337–404, ISSN 0002-9947.

[2] Bay, H., Ess, A., Tuytelaars, T., and Van Gool, L., 'Speeded-up robust features (surf),' Computer vision and image understanding, 2008, **110**(3), pp. 346–359.

[3] Bruck, H. A., McNeill, S. R., Sutton, M. A., and Peters, W. H., 'Digital image correlation using Newton-Raphson method of partial differential correction,' Experimental mechanics, 1989, **29**(3), pp. 261–267, ISSN 0014-4851.

[4] Calonder, M., Lepetit, V., Strecha, C., and Fua, P., 'Brief: Binary robust independent elementary features,' in 'European conference on computer vision,' Springer, 2010 pp. 778–792.

[5] De Strycker, M., Schueremans, L., Van Paepegem, W., and Debruyne, D., 'Measuring the thermal expansion coefficient of tubular steel specimens with digital image correlation techniques,' Optics and Lasers in Engineering, 2010, **48**(10), pp. 978–986, ISSN 0143-8166.

[6] Eberl, C., Gianola, D. S., and Hemker, K. J., 'Mechanical characterization of coatings using microbeam bending and digital image correlation techniques,' Experimental mechanics, 2010, **50**(1), pp. 85–97, ISSN 0014-4851.

[7] Eshtayeh, M., Hijazi, A., and Hrairi, M., 'Nondestructive Evaluation of Welded Joints Using Digital Image Correlation,' Journal of Nondestructive Evaluation, 2015, **34**(4), pp. 1–12, ISSN 1573-4862, doi:10.1007/s10921-015-0310-z.

[8] Grant, B. M. B., Stone, H. J., Withers, P. J., and Preuss, M., 'High-temperature strain field measurement using digital image correlation,' The Journal of Strain Analysis for Engineering Design, 2009, **44**(4), pp. 263–271, ISSN 0309-3247.

[9] Horaud, R., Forbes, F., Yguel, M., Dewaele, G., and Zhang, J., 'Rigid and articulated point registration with expectation conditional maximization,' IEEE Transactions on Pattern Analysis and Machine Intelligence, 2011, **33**(3), pp. 587–602.

[10] Lewis, J. P., 'Fast normalized cross-correlation,' in 'Vision interface,' volume 10, 1995 pp. 120–123.

[11] Lowe, D. G., 'Object recognition from local scale-invariant features,' in 'Computer vision, 1999. The proceedings of the seventh IEEE international conference on,' volume 2, Ieee, 1999 pp. 1150–1157.

[12] Ma, J., Jiang, J., Gao, Y., Chen, J., and Liu, C., 'Robust image matching via feature guided Gaussian mixture model,' 2016 IEEE International Conference on Multimedia and Expo (ICME), 2016, pp. 1–6, doi:10.1109/ICME.2016.7552867.

[13] Ma, S., Zhao, Z., and Wang, X., 'Mesh-based digital image correlation method using higher order isoparametric elements,' The Journal of Strain Analysis for Engineering Design, 2012, **47**(3), pp. 163–175, ISSN 0309-3247.

[14] Mekky, W. and Nicholson, P. S., 'The fracture toughness of Ni/Al2O3 laminates by digital image correlation I: Experimental crack opening displacement and R-curves,' Engineering Fracture Mechanics, 2006, **73**(5), pp. 571–582, ISSN 00137944, doi: 10.1016/j.engfracmech.2005.09.005.

[15] Myronenko, A. and Song, X., 'Point set registration: Coherent point drift,' IEEE transactions on pattern analysis and machine intelligence, 2010, **32**(12), pp. 2262–2275.

[16] Pan, B., 'Reliability-guided digital image correlation for image deformation measurement,' Applied optics, 2009, **48**(8), pp. 1535–1542.

[17] Pan, B., Dafang, W., and Yong, X., 'Incremental calculation for large deformation measurement using reliability-guided digital image correlation,' Optics and Lasers in Engineering, 2012, **50**(4), pp. 586–592.

[18] Pan, B., Li, K., and Tong, W., 'Fast, Robust and Accurate Digital Image Correlation Calculation Without Redundant Computations,' Experimental Mechanics, 2013, **53**(7), pp. 1277–1289, ISSN 1741-2765, doi:10.1007/s11340-013-9717-6.

[19] Pan, B., Qian, K., Xie, H., and Asundi, A., 'Two-dimensional digital image correlation for in-plane displacement and strain measurement: a review,' Measurement science and technology, 2009, **20**(6), p. 62001, ISSN 0957-0233.

[20] Pan, B., Wang, B., and Lubineau, G., 'Comparison of subset-based local and fe-based global digital image correlation: Theoretical error analysis and validation,' Optics and Lasers in Engineering, 2016, **82**, pp. 148–158.

[21] Pan, B., Wu, D., Wang, Z., and Xia, Y., 'High-temperature digital image correlation method for full-field deformation measurement at 1200 C,' Measurement science and technology, 2010, **22**(1), p. 15701, ISSN 0957-0233.

[22] Pan, B., Xie, H., and Wang, Z., 'Equivalence of digital image correlation criteria for pattern matching,' Applied optics, 2010, **49**(28), pp. 5501–5509.

[23] Pan, B., Xie, H., Xu, B., and Dai, F., 'Performance of sub-pixel registration algorithms in digital image correlation,' Measurement Science and Technology, 2006, **17**(6), p. 1615.

[24] Peters, W. H. and Ranson, W. F., 'Digital Imaging Techniques In Experimental Stress Analysis,' Optical Engineering, 1982, **21**(3), pp. 213427–213427, ISSN 0091-3286.

[25] Rosten, E. and Drummond, T., 'Machine learning for high-speed corner detection,' in 'European conference on computer vision,' Springer, 2006 pp. 430–443.

[26] Rublee, E., Rabaud, V., Konolige, K., and Bradski, G., 'Orb: An efficient alternative to sift or surf,' in 'Computer Vision (ICCV), 2011 IEEE International Conference on,' IEEE, 2011 pp. 2564–2571.

[27] Sánchez-Arévalo, F. and Pulos, G., 'Use of digital image correlation to determine the mechanical behavior of materials,' Materials Characterization, 2008, **59**(11), pp. 1572–1579, ISSN 10445803, doi:10.1016/j.matchar.2008.02.002.

[28] Sedaghat, A., Mokhtarzade, M., and Ebadi, H., 'Uniform robust scale-invariant feature matching for optical remote sensing images,' IEEE Transactions on Geoscience and Remote Sensing, 2011, **49**(11), pp. 4516–4527.

[29] Sun, Y., Pang, J. H. L., Wong, C. K., and Su, F., 'Finite element formulation for a digital image correlation method,' Applied optics, 2005, **44**(34), pp. 7357–7363, ISSN 1539-4522.

[30] Tsai, D.-M. and Lin, C.-T., 'Fast normalized cross correlation for defect detection,' Pattern Recognition Letters, 2003, **24**(15), pp. 2625–2631, ISSN 0167-8655.

[31] Verstraete, M., Denys, R., Van Minnebruggen, K., Hertelé, S., and De Waele, W., 'Determination of CTOD resistance curves in side-grooved Single-Edge Notched Tensile specimens using full field deformation measurements,' Engineering Fracture Mechanics, 2013, **110**, pp. 12–22, ISSN 00137944, doi:10.1016/j.engfracmech.2013.07.015.

[32] Wang, B., Pan, B., and Lubineau, G., 'Some practical considerations in finite element-based digital image correlation,' Optics and Lasers in Engineering, 2015, **73**, pp. 22–32.

[33] Wang, Z., Vo, M., Kieu, H., and Pan, T., 'Automated Fast Initial Guess in Digital Image Correlation,' Strain, 2014, **50**(1), pp. 28–36, ISSN 00392103, doi:10.1111/str.12063.

[34] Wu, R., Kong, C., Li, K., and Zhang, D., 'Real-time digital image correlation for dynamic strain measurement,' Experimental Mechanics, 2016, **56**(5), pp. 833–843.

[35] Zhao, J.-q., Zeng, P., Lei, L.-p., and Ma, Y., 'Initial guess by improved population-based intelligent algorithms for large inter-frame deformation measurement using digital image correlation,' Optics and Lasers in Engineering, 2012, **50**(3), pp. 473–490.

[36] Zhou, Y. and Chen, Y. Q., 'Feature matching for automated and reliable initialization in three-dimensional digital image correlation,' Optics and Lasers in Engineering, 2013, **51**(3), pp. 213–223, ISSN 01438166, doi:10.1016/j.optlaseng.2012.10.011.

[37] Zhou, Y., Pan, B., and Chen, Y. Q., 'Large deformation measurement using digital image correlation: a fully automated approach,' Applied optics, 2012, **51**(31), pp. 7674–7683, ISSN 1539-4522.

II. BISECTION SEARCHING BASED REFERENCE FRAME UPDATE STRATEGY FOR DIGITAL IMAGE CORRELATION

Yunlu Zhang

Department of Mechanical & Aerospace Engineering

Missouri University of Science and Technology

Rolla, Missouri 65409–0050

Email: yzdyf@mst.edu

ABSTRACT

The strategy to update the reference frames in the digital image correlation (DIC) analysis is an essential but often overlooked problem. A good reference frame update strategy should be able to adjust the frame step in respect of varying practical circumstances including the different loading rate, speckle pattern, plastic deformation, imaging system, lighting condition, etc. In this work, a simple but effective bisection searching (BS) strategy is presented to solve this problem. The frame step is reduced into one half for the unconverged locations, and the intermediate frame is utilized to assist the correlating process. This process is iteratively conducted to adjust the frame step in different regions automatically. The performance of the BS strategy is evaluated against the constant step (CS) update strategy on simulated experiments. The results indicate that the BS strategy can automatically adjust the frame step for changing speckle pattern and loading rate. The accuracy and robustness of the BS strategy are better than the CS strategy with the same pixel level and subpixel level searching algorithms. The BS strategy also successfully tracked all POIs and adjusted the frame step in the real world experiment with changing loading rate and large plastic deformation (over 70% engineering strain).

Keywords: digital image correlation, template update, reference frame update, bisection method

1. INTRODUCTION

The objective of digital image correlation (DIC) analysis is to track the positions of predefined points, i.e., points of interest (POIs), on the surface of the specimen from the initial state to the last state. From the displacement information of these POIs, 2D or 3D surface deformation, strain field, elongation, crack tip opening displacement, the coefficient of thermal expansion, and other useful quantities could be derived [7].

DIC may be considered as one of visual object tracking algorithms. However, unlike most visual tracking algorithms proposed in computer vision community that only output the positions of bounding box with the expected accuracy of several pixels, the experimental metrology applications require the results from DIC are accurate at the subpixel level. Much research effort has been devoted to improving the accuracy of subpixel level searching algorithm. Inverse compositional Gauss-Newton algorithm (IC-GN) [11] is the most widely adopted subpixel level searching algorithm due to its high accuracy and efficiency. Recently, Zhou *et al.* [18] proposed an offset subset modification to reduce the systematic error and eliminate subpixel interpolation in the reference image. Su *et al.* [13] aimed to solve the same problem by introducing position randomness to the subset. For pixel level searching, Zhang *et al.* [17] suggested a robust feature matching based point set registration approach to generate the accurate initial guess for all POIs in cases with small or large translation, deformation, or rotation.

The surface patterns that carry the deformation information may change considerably due to many unavoidable factors. The first common situation is that new surface features appear under large plastic deformation, such as PortevinâĂŞLe Chatelier effect. Another case is that the thermal radiation of the specimen at high temperature changes the

surface feature. The varied surface pattern makes it extremely difficult if not impossible to directly find the corresponding locations in the last frame from the initial frame, e.g., the decorrelation effect occurs [10].

However, only limited researches have been committed to solving this problem. One trivial solution would be changing the reference frame at a constant frame step, e.g., the constant step strategy (CS). Nevertheless, the selection of the appropriate step is not a trivial problem. If the step is too large, the decorrelation could still happen. If the step is too small, the small error generated at each reference frame calculation will be accumulated, and the results would not be accurate. Besides, the CS strategy could not account for varying conditions including loading rate, illumination, noise level, etc.

Pan *et al.* [10] proposed an incremental reliability guided (IRG) technique regarding this problem. The reliability guided method was introduced in [6] that the initial guess for every POI is from the converged deformation parameter of its neighbors with the highest zero normalized cross-correlation coefficient (ZNCC). The initial guess of the first POI, called the seed point, is from integer pixel displacement searching. The IRG strategy determines a new reference frame has to be used only when the ZNCC of the seed point is smaller than a predefined threshold. Tang *et al.* [15] suggested another approach. They utilized the deformation parameter of the seed point in $(n-1)$th frame to initialize the shape of the subset in the reference frame and then match it in the nth frame. This method is quite similar to the template update strategy in visual tracking area [5]. It is equivalent to use the deformation parameter in the $(n-1)$th frame as the initial guess for the nth frame. The reference frame update criterion in [15] is the standard deviation of grayscale residual larger than a predefined value. Another approach called the single step DIC was proposed by Goh *et al.* [4]. The loading force and displacement are used to estimate the deformation parameter and initiate subpixel level searching. They claimed that it does not need to update the reference frame.

Although these methods are more flexible than the CS strategy, each one has its limitation. One obvious drawback of the IRG strategy is that each time only the ZNCC of one or several seed points was examined to determine if the reference frame need be updated. It could not guarantees all other POIs could be successfully matched with this frame step due to the possible large local deformation. Also, the IRG strategy uses the $(n-1)$th frame as the current frame if the calculated ZNCC of the seed point in the nth frame is below the threshold. This strategy of reducing the frame step may present a performance issue that several consecutive current frames may all fail due to their similar states. In [15], the physical meaning of the criterion of the standard deviation of the grayscale residual is not clear. Single step DIC [4] only works for the elastic deformation situation like the rubber used in the experiment and replies on additional loading data.

Currently, one trend in the DIC experiments is that the analyzed data is only a small part of the captured data. For instance, the most industrial camera could output full resolution images at a rate of 10 to 30 frame per second. In the current work, a bisection searching (BS) strategy is proposed to tackle the reference frame update problem in DIC by utilizing the abundant recorded images. The intermediate frame is automatically utilized to assist the correlation calculation. In this way, the frame step is reduced only for those POIs with large deformation or varying surface pattern. Also, the frame step is kept at a high value for other POIs to reduce the accumulated error. The idea of utilizing the abundant images coincides with the recently proposed spatial-temporal DIC [3], which exploits the information on the neighboring frames to improve the accuracy of DIC algorithm.

The rest of the paper is organized as follows. The BS strategy is detailed in Section 2. The effectiveness of this strategy is studied in the simulated and real-world experiments in Section 3. Finally, conclusions are drawn in Section 7.

2. BISECTION SEARCHING BASED REFERENCE FRAME UPDATE STRATEGY

2.1. BASIC PRINCIPAL OF DIGITAL IMAGE CORRELATION

Only necessary concepts of DIC analysis are presented in this subsection. For a detailed discussion, the readers are referred to [11] and [1] and reviews [12] and [9]. Here subset based IC-GN DIC is presented. However, It should be noted that the BS strategy could also be used with other subset-based or fullfield-based DIC algorithms.

Subset-based DIC algorithm can be considered as one of the area-based image registration/matching method. DIC algorithm tracks the locations POIs at different stages of the deformation with know locations in the initial stage. For each POI, it actually represents a small square image around it, and the small image is designated as the subset. The image frame that contains POIs with known locations is the reference frame, and the image frame to find the deformed locations of POIs is the current frame. To describe the deformation of a subset, the first-order approximation is often adopted. In other words, the displacement and the gradient of the displacement are to be assumed as constant within the subset. It could be expressed as

$$\begin{aligned} x^* &= x + u + u_x(x - x_0) + u_y(y - y_0) \\ y^* &= y + v + v_x(x - x_0) + v_y(y - y_0) \end{aligned} \tag{1}$$

where (x, y) is the coordinate of a point of the subset in the reference frame, (x^*, y^*) is the coordinate of the corresponding point in the current frame, (x_0, y_0) is the coordinate of the center of the subset, e.g, POI, in the reference frame, u, v and u_x, u_y, v_x, v_y are the displacements and gradients of displacement within the subset, $p = (u, v, u_x, u_y, v_x, v_y)$ is the set of deformation parameter that needs to be estimated.

To quantify the similarity between two subsets, the criterion of zero-mean normalized sum of squared difference (ZNSSD) is widely adopted. The ZNSSD coefficient of two subsets is

$$C_{\mathrm{ZNSSD}}(\boldsymbol{p}) = \sum_{\Omega} \left(\frac{(F(x,y) - \bar{F})}{\Delta F} - \frac{(G(x^*,y^*) - \bar{G})}{\Delta G} \right)^2 \tag{2}$$

where Ω is the set of points in the subset, $F(x,y)$ and $G(x^*,y^*)$ are intensity values of the points in the reference and current frame. It should be noted that both (x,y) and (x^*,y^*) could be at subpixel positions, so interpolation is required. $\Delta F = \sqrt{\sum_{\Omega}(F(x,y) - \bar{F})^2}$ and $\Delta G = \sqrt{\sum_{\Omega}(G(x^*,y^*) - \bar{G})^2}$ are the fluctuations in the subsets, and $\bar{F}$ and $\bar{G}$ are mean intensity values of the subsets. The possible range of C_{ZNSSD} is $[0,4]$ and the lower the C_{ZNSSD} represents higher the similarity between the two subsets.

The objective of DIC to find the corresponding point in the current frame is accomplished by finding the deformation parameter p that minimizes the ZNSSD criterion. The optimal deformation parameter p can be calculated by the gradient-based iterative algorithms, and IC-GN is one of them. The estimated difference of deformation the parameter is

$$\Delta p = -\frac{\nabla C_{\mathrm{ZNSSD}}(\boldsymbol{p}_0)}{\nabla\nabla C_{\mathrm{ZNSSD}}(\boldsymbol{p}_0)} \tag{3}$$

where $\boldsymbol{p}_0$ is the initial value of the deformation parameter or the result from the previous iteration.

As the nature of the gradient-based method, it could only converge to the local optimum. Therefore, to get the correct subpixel level deformation parameter, an initial guess close to global optimum should be provided to the subpixel level searching algorithm. This step is called pixel level searching. The integer pixel searching method is commonly adopted. This algorithm calculates the cross-correlation coefficient of a subset at candidate positions locate around the POI. The integer displacement to the location with the highest cross-correlation coefficient will be the initial guess. However, it suffers from the drawback that failure may happen in the cases of rotation or non-rigid deformation. Recently, a

feature matching based point set registration approach was proposed to generate subpixel level accurate initial guess for all POIs even in cases with rotation and nonrigid deformation [17].

2.2. BISECTION SEARCHING

The previous subsection only discussed the tracking problem between two frames. However, in practice, multiple image frames or a continuous video are often used to record the changing states of the specimen. The first benefit of this approach is that the deformation information at these intermediate states can be determined, which may provide useful insights. As will be demonstrated, the result in the intermediate state can assist the tracking process to the last frame. In considering the tracking problem of multiple frames, let

$$\boldsymbol{X}^i = \begin{pmatrix} x_0^i & y_0^i \\ x_1^i & y_1^i \\ \cdots & \cdots \\ x_{n-1}^i & y_{n-1}^i \end{pmatrix} \tag{4}$$

where $\boldsymbol{X}^i$ stores the coordinates of all POIs at the frame of index i, $i \in [0, 1, \cdots, m-1]$, m is the total number of frames, n is the total number of POIs.

As discussed previously, always use the initial frame as the reference frame only works for small deformation cases, and it is not suitable for many practical situations. In contrast, always update the reference frame at a constant step also generate the large accumulated error if the frame step is too small, and the calculation may fail if the frame step is too large. Meanwhile constant frame step could not be adapted to varying situations.

In principle, a feedback control strategy could be used to solve this problem, which is similar to the time stepping algorithm in finite element analysis. However, in general, the dynamic model of the DIC error in respect to frame step is not clear, and it is also dynamic and nonlinear with changing situations. Therefore, this approach is not considered here.

A simple yet effective reference frame update strategy is introduced to solve these issues. This strategy is similar to the bisection method in root finding. Therefore it is called the bisection searching strategy. It tries to directly track the POIs from the initial frame to the last frame. If it fails, then reduce frame step in half and this process continuous recursively. As illustrated in Figure 1, with known POIs $\boldsymbol{X}^0$, the first step is to find the corresponding locations $\boldsymbol{X}^{100}$ and if it fails, then it tries to track the POIs from frame 0 to frame 50 and from 50 to frame 100. During these two sub-steps, the same strategy is applied if any step could not converge. The criterion to determine if the tracking step fails or not is discussed later. In this way, the frame step reduces automatically in the hard to converge steps, and the frame step keeps at the high value in the period with small differences.

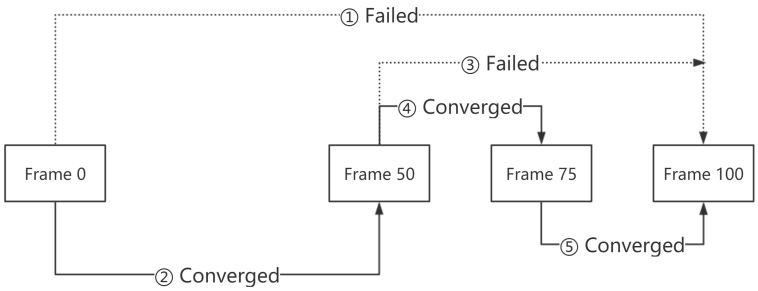

Figure 1. Schematic illustration of the BS strategy in finding appropriate reference frames. The circled numbers are the order of calculation. Dotted lines and solid lines represent failed attempts and successful tracking respectively.

Once the reference frames are determined, they can be utilized as landmarks to derive additional displacement at the required frame indexes. These additional frames together with the reference frames are called output frames. Figure 2 shows the calculation of additional output frames at the required frame step of 10. Since the tracking calculation succeeded between the reference frames, it is expected to converge with smaller frame step at the output frame. A two-step procedure is proposed to reduce the need for pixel level searching during output frame calculation by utilizing the calculated displacement information. First, a similar bisection searching step is conducted to generate denser frame indexes with maximum frame step less or equal to the desired output step. As Figure 2

shown, additional results at frames 57, 63, and 69 are generated. Here dotted lines represent the initial guess of deformation parameters are estimated by linear interpolation. It should be noted that all the reference frame, in this case, is still the frame 50. The second step is to calculate the frames at the required step if they are not available yet. The procedure is similar to the previous step by using the linear interpolation to get the initial guess. A full pixel and subpixel level searching will be carried if the number of not converged POIs is larger than the number calculated from the original reference frames (in this case is from frame 50 to frame 75). The last subfigure shows the overall reference frame calculation relationship. For all additional output frames, it is directly calculated from its previous reference frame. In this way, the dense output information is derived, and the accumulated error is minimized.

Regarding the criterion of successful tracking, Figure 3 illustrates the detailed procedure for a typical combination of pixel and subpixel level searching algorithm. With known POIs $\boldsymbol{X}^i$, the first step is to determine if the pixel level searching failed. For the feature based point set registration algorithm [17], the convergence criterion is that the change of estimated deformation field is smaller than a threshold within a certain number of iterations. If it fails, the same BS strategy is utilized on the reduced frame step and recursively solves for all POIs. The middle index $(i + j)/2$ is rounded to the nearest integer in the calculation.

If the pixel level searching is successful, then subpixel level searching is followed with the determined initial guess. The convergence criterion of IC-GN algorithm is the norm of the change of the displacement is less than a threshold within a certain number of iterations [8]. Also, the POI is considered not converged if its C_{ZNSSD} is larger than a threshold C_{th}. The combined criteria of convergence and C_{th} could effectively eliminate the false matching. The subpixel level calculation of each POI is independent, so it is possible that a part of POIs converged and others are not. For those unconverged POIs, the possibility of moving out of frame should be considered. Here a simple test is adopted. If the distance

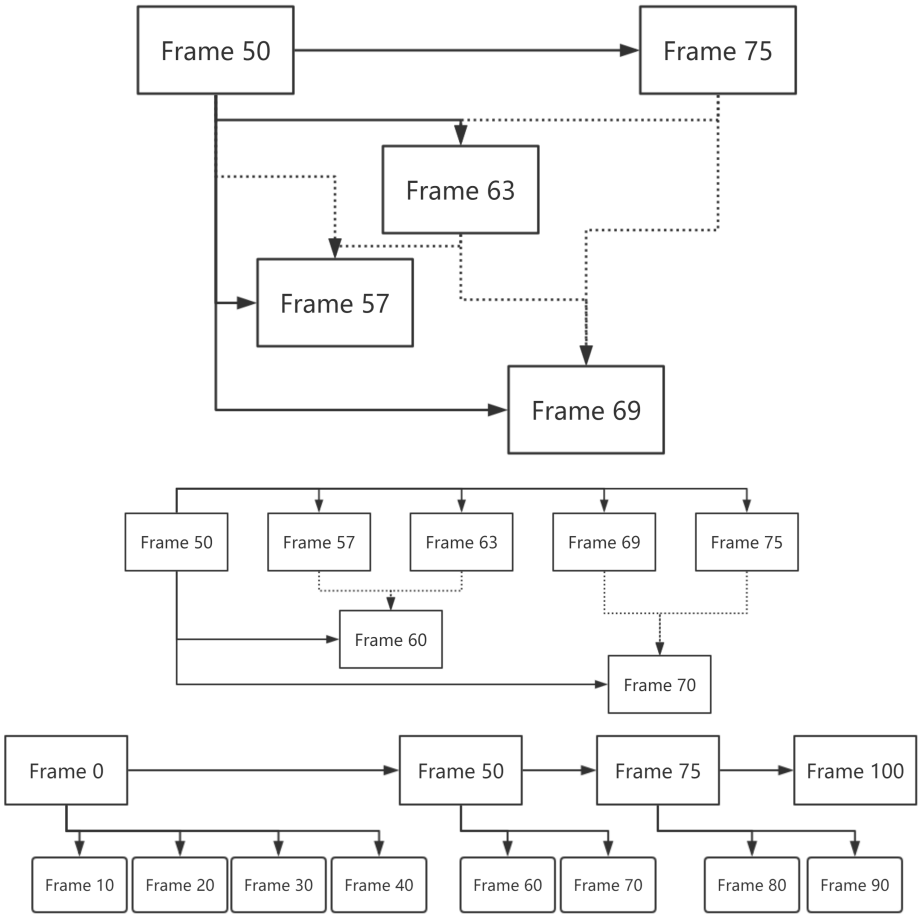

Figure 2. Schematic illustration of the strategy to derive additional deformation information at output frames. Solid lines represent the calculation from the reference frame to current frame. Dotted lines represent the linear interpolation to provide an initial guess of deformation parameters.

of any point in the estimated deformed subset to the boundary of the image is less than 5 px in the current frame or any point is actually out of the field of the image, the corresponding POI is marked as out of the field and not considered as unconverged. The 5 px margin is set for the support domain of interpolation. If there is not any unconverged POI, then the locations of all POIs $\boldsymbol{X}^j$ at frame j is obtained. Otherwise, a test of current frame step is conducted. If the current frame step $j - i$ is only 1, then the not fully converged result has to be returned to terminate the recursive function. If the frame step is larger than 1, next the ratio of the number of current unconverged POIs to the number of previously valid

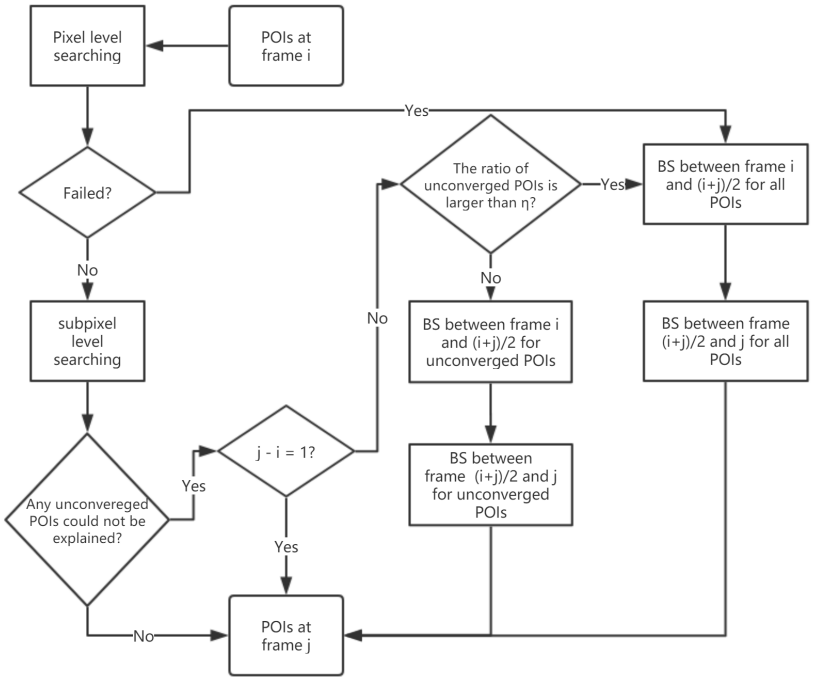

Figure 3. Schematic illustration of the complete steps of the BS strategy. It consists of the failure criteria of pixel and subpixel level searching algorithm and the corresponding procedure under different cases.

POIs determines if a bisection searching need to be conducted on all POIs or only on the unconverged POIs. If the ratio is larger than a threshold η, it indicates that a large number of initial guesses are not accurate or the tracking patterns changed considerably, so the subpixel level searching algorithm could not converge. Then a bisection searching is conducted on all POIs. On the other hand, if only a small amount of POIs could not converge, then to avoid introducing accumulated error for most POIs, the bisection searching is only conducted on these POIs.

2.3. IMPLEMENTATION NOTES

In total, there are only two hyper-parameters need to be set in the BS strategy except the parameters for the pixel and subpixel level searching algorithms: the ZNSSD threshold C_{th} and the unconverged ratio threshold η. They were set to 0.2 and 0.1 respectively in the

implementation. The threshold of C_{th} of 0.2 equals the requirement of ZNCC coefficient should be larger than 0.9, which is more strict than the threshold C_{ZNCC} of 0.8 in [10]. The unconverged ratio threshold η is another empirical parameter that determines how often the complete bisection searching is conducted. If this threshold is too small, unnecessary bisection searching will be conducted on the POIs that already converged with the larger frame step and resulted in a higher accumulated error. If this threshold is too large, it could not effectively exclude obvious faulty initial guess that does not converge for a large number of POIs.

The original point set registration algorithm used in [17] was the feature guided Gaussian mixture model. It has been switched to the adaptive vector field consensus point set registration method [16]. The latter method automatically determines the suitable regularization parameter and is more robust and versatile.

The adaptive subset algorithm was used instead of the original IC-GN algorithm [18]. The advantage is that it eliminates the interpolation step for the POIs at the subpixel locations, increases the efficiency, and reduces the systematic error.

3. EXPERIMENTS AND RESULTS

The performance of the BS strategy was compared with the CS strategy on two simulated experiments. Also, the BS strategy was also applied to a real-world experiment. The IRG strategy was not compared here due to its limitation discussed in the introduction and incompatibility between the reliability guided approach and the feature matching based pixel level searching algorithm.

3.1. SIMULATED EXPERIMENTS

The deformation of two simulated experiments was the large degree of pure rotation, which is hard to track for the DIC algorithm. The rotation processes were both divided into two stages with different characteristics. The difference is that in the first experiment, the varying factor is the speed of rotation. The time duration ratio and speed ratio in the two stages are $2:1$ and $1:6$ respectively. In this way, the adaptability of the reference frame update strategy under varying loading rate was evaluated. In the second experiment, the actual speckles were replaced gradually to simulate the varying speckle pattern in the plastic deformation situation. 6% of speckles were moved to new random locations following uniform distribution at the last frame. The replacing process was also divided into two stages and the time duration ratio and replacement rate ratio in two stages were also $2:1$ and $1:6$ respectively. The rate of rotation in this experiment was kept as constant. The specific values of these parameters were set by preliminary experiments that ensure the moderate amount of bisection searching is required, and the total computation time is not too long. The change of the varying factor to the frame index is shown in Figure 5. The size of the generated images was 500×500 px, and the maximum degree of rotation in the two experiments were $\pi/2$ and $\pi/4$ respectively. The number of simulated images was 300. Some represent frames of generated speckle images are shown in Figure 4.

The algorithm to generate the speckle images was the Boolean model [14]. This algorithm simulates the process of image acquisition chain and eliminates the need for interpolation. The bit depth of the simulated speckle image was 8. The standard deviation of the Gaussian point spread function σ was 0.5. The quantization error probability α was set to 0.1. The contrast of the image γ was set to 0.9. These parameters were adopted from the original paper that can generate realistic speckle patterns within practical computation time. The original paper used the Poisson process to get the locations of the speckles. In this work, it was replaced by a newly improved artificial pattern [2]. The randomness parameter and radius of the speckle were set to 0.3 and 2 px respectively.

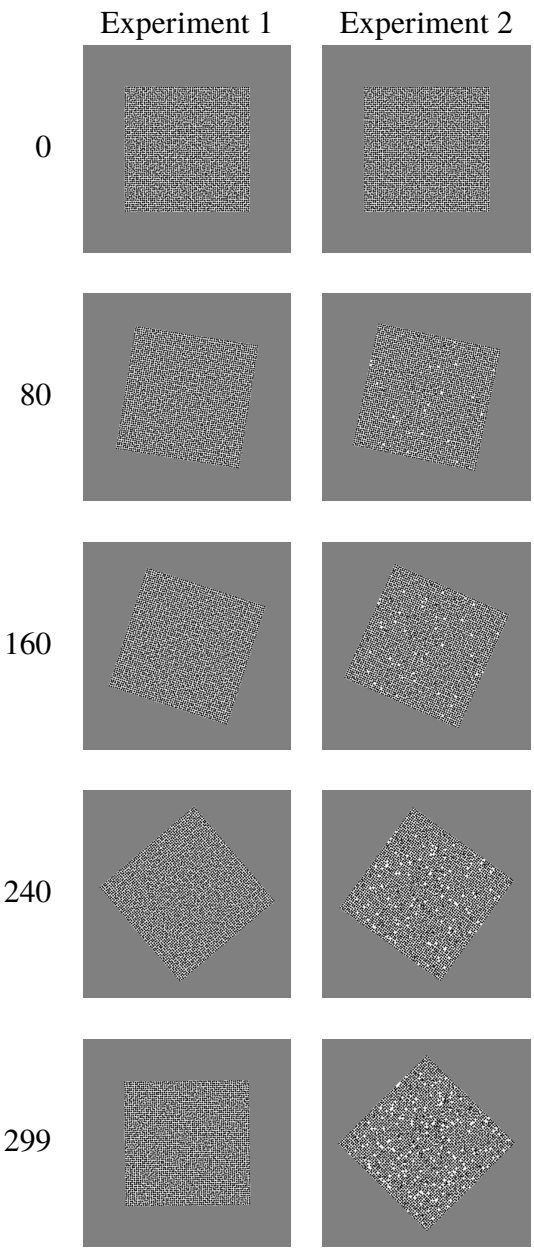

Figure 4. Simulated speckle images under the rotation deformation. The number on the left is the frame index of the images.

In experiment 1, the BS strategy was compared with the CS strategy with frame step from 10 to 100 with the step of 10. The pixel and subpixel level searching algorithm used by these strategies were the same. 784 POIs were evenly distributed in the square with the grid step of 10 px. The subset size was 21×21 px. The number of maximum IC-GN iterations was 25.

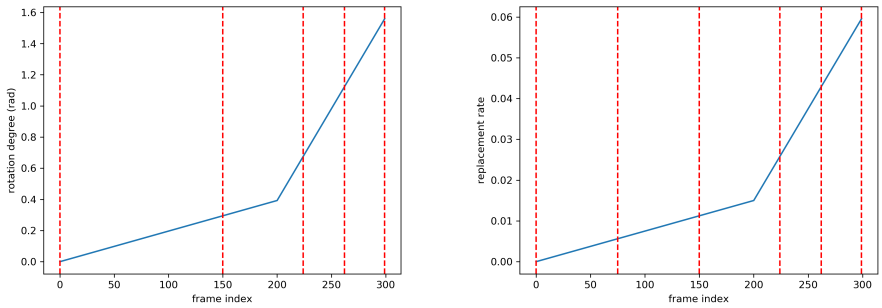

(a) Experiment 1 (b) Experiment 2

Figure 5. The relationship between the varying factor and the frame index in the simulated experiments. The vertical dashed lines represent the locations of reference frames determined by the BS strategy. The y axis represents (a) degree of rotation, (b) replace rate.

All strategies except the CS strategy of frame step 100 were able to generate converged results $\boldsymbol{X}^{299}$ for all POIs at the last frame. The CS strategy of step 100 generated 775 failed POIs when calculating from frame 200 to 299. Root of mean squared error (RMSE) was utilized to measure the difference of determined displacement to the commanded displacement at the last stage. The results are summaries in Table 1. The BS strategy performed the best with the lowest RMSE among all results. The determined frame steps were 150, 74, 38, and 37 respectively as shown in Figure 5. The BS strategy automatically reduced the frame step at the period of the higher rotation rate. The CS strategy with the frame step of 80 produced the minimum RMSE among CS strategies. If the frame step is small, the accumulated error causes the increase of RMSE. If the frame step is too large, the DIC algorithm could not successfully track all POIs. This result confirms the previous analysis of the CS strategy. As shown in Table 1, the computation time of CS strategies decreased with the increase of the frame step. The computation time of the BS strategy was 11.4s and was close to that of the CS strategy with frame step of 30. Although the computation time of CS was higher than some CS strategies, it avoids the time-consuming process of manual selection of the frame step in the CS strategy.

Table 1. RMSE and computation time of the BS strategy and CS strategy with different frame step in the simulated experiment 1.

	BS	CS 10	CS 20	CS 30	CS 40	CS 50
RMSE (px)	0.0045	0.0564	0.0096	0.0068	0.0061	0.0052
Computation time (s)	11.4	29.6	15.1	10.5	8.7	6.8
	CS 60	CS 70	CS 80	CS 90	CS 100	
RMSE (px)	0.0053	0.0050	0.0046	0.0057	failed	
Computation time (s)	5.9	6.0	5.0	4.9		

In experiment 2, the BS strategy was compared with the CS strategy with the frame step from 10 to 40 with the step of 10. The locations and number of POIs were the same as experiment 1. The DIC analysis was harder to converge and resulted RMSEs were higher than experiment 1 due to the replacement of speckles. The CS strategy with frame step 40 was failed to get the result. The automatic determined locations of the reference frames is shown in Figure 5(b). The BS strategy also automatically decreased the frame step in the region with larger speckle replacement rate, and the average frame step was 60, which was larger than the CS strategies. None of the strategies generated all converged POIs. Among them, the BS strategy solved 782 out of 784 POIs, and the number of solved POIs by the CS strategy decreases as the frame step increase. At first glance, RMSE of the BS strategy was larger than RMSEs of the CS strategy with step 20 and 30. In fact, this is not a fair comparison due to the BS strategy converged at those POIs the CS strategy could not. The subsets of these POIs contains removed or added speckles that will interfere with the tracking process. Therefore, a new intersection RMSE was computed among the intersection of all converged POIs from all strategies. The result shows that the BS strategy was the best on all converged POIs. The RMSE of the CS strategy increases with the decrease of the frame step due to the accumulated error.

Table 2. RMSE, number of converged POIs, and computation time of the BS strategy and CS strategy with different frame step in the simulated experiment 2. Intersection RMSE means the RMSE were computed among the intersection of all converged POIs from all strategies.

	BS	CS 10	CS 20	CS 30	CS 40
RMSE (px)	0.0431	0.0576	0.0415	0.0408	failed
Num. of converged POIs	782	737	693	665	
Intersection RMSE (px)	0.0400	0.0559	0.0406	0.0406	
Computation time (s)	25.1	29.4	15.0	10.4	

The computation time of the BS strategy was less than the CS strategy with frame step of 10 and larger than the rest CS strategies. This is because the total number of the BS computation iterations was 29, which includes all failed trials and partial computations. The higher computation time of the BS strategy was reasonable and necessary to automatically adjust the frame step and increase the number of solved POIs.

3.2. REAL-WORLD EXPERIMENT

The effectiveness of the BS strategy was also validated on a tensile test. Because in the realistic experiment, there is no true deformation information available to test the accuracy. So only the adaptability of the BS strategy was tested here. Similar to the simulated experiment 1, the loading rate was increased dramatically during the test: changed from 1.67×10^{-3}mm/s to 1.67×10^{-2}mm/s. The material of the specimen was highly ductile pure copper. The length, width, and thickness of the gauge section were 3 mm, 1 mm, and 1 mm respectively. The total testing time was 6 min. A continuous video with the frame rate of 30 was used to record the progress of deformation. The natural scratches on the surface of the specimen were used as the pattern to track the deformation. The grid step of POIs and subset size were 15 px and 21×21 px respectively. The total number of POIs was 690.

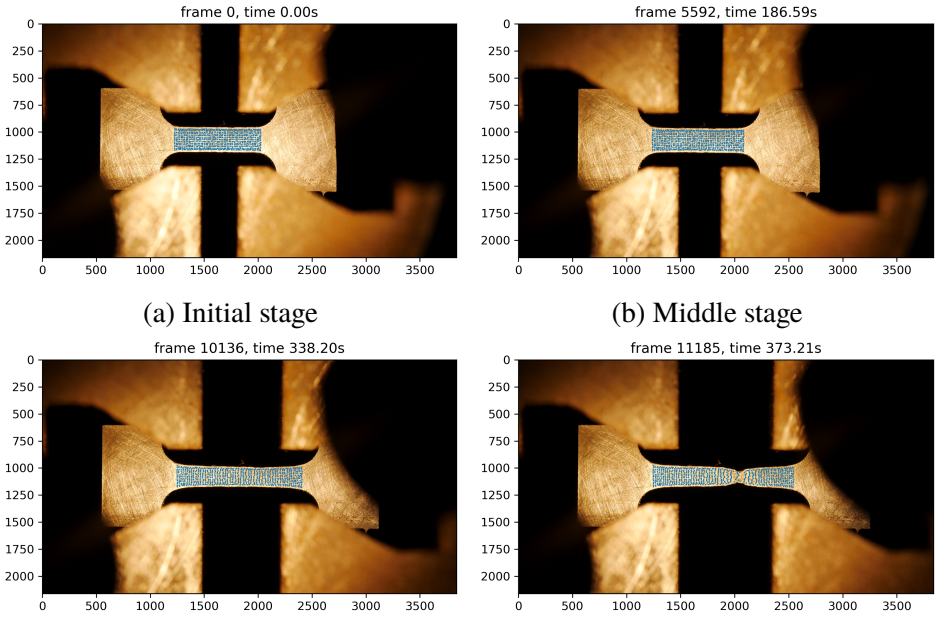

(a) Initial stage (b) Middle stage

(c) Necking start (d) Final stage

Figure 6. Tracked POIs on the tensile specimen at four representative stages.

The BS strategy successfully tracked all POIs from the initial frame to the last frame before the fracture. Four representative frames and corresponding POIs are shown in Figure 6. Additional output frames were calculated at the frame step of 30. The derived elongation is plotted in Figure 7 along with the locations of determined reference frames. The elongation could be divided into three regions. The first flat region corresponds to the stage before the tensile test starts. The second and third regions are the slow and fast loading periods respectively. It shows clearly that the BS strategy automatically reduced frame step in the high loading rate period to ensure convergence, and used large frame step in the small loading rate region to reduce the accumulated error.

In the large loading rate region, the frame step was not constant, and it can be divided into three sub-regions. The first sub-region may be attributed to the response of the rapid loading rate change, and the last region may relate to the necking process. To validate this hypothesis, the volume consistent factor (VFC) is plotted with respect to the frame index in

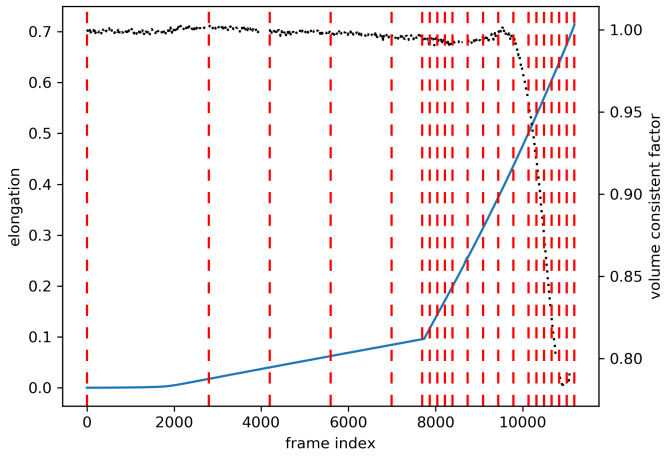

Figure 7. The relationship between the elongation, volume consistent factor, and the determined reference frames. Solid line, dotted line, and vertical dashed lines represent the elongation, volume consistent factor, and locations of generated reference frames respectively.

Figure 7. VFC is defined as

$$\mathrm{VCF} = (1 + \epsilon)(w/w_0)^2 \tag{5}$$

where ϵ is the elongation, w is the width of the specimen, w_0 is the initial width. The width was calculated from the minimum distance between the upper and lower boundary of the POIs. When the specimen was under uniform deformation, the volume consistent constraint should hold, and VFC should be close to 1. The larger the deviation of VFC from 1 represents the higher degree of local deformation, e.g., the necking process. Figure 7 shows clearly that the third sub-region coincides with the rapid decrease of VFC, which indicates that BS strategy automatic reduced the frame step for the large local deformation. The corresponding deformation state at frame 10136 is shown in Figure 6(c).

4. DISCUSSION

Previous results indicate that the BS strategy is capable of adjusting the frame step for the changing loading rate and speckle pattern. Although the BS strategy may not generate the optimal reference frames among all possible routes, it shares the same characters of simplicity and robustness as the counterpart in root finding. The uniqueness of the BS strategy includes the minimal number of hyper-parameters and the adaptability to changing situations. It should be noted that the BS strategy does not aim to replace any existing pixel level and subpixel level DIC searching algorithms. However, it will work with most DIC algorithms with minor modifications and improve the robustness and accuracy of DIC analysis. For instance, the strategy of reducing the frame step in IRG algorithm can be replaced with the BS strategy to avoid the possible performance issue discussed in the introduction.

It should be noted that all the previous analysis of the BS strategy was based on the monotonic loading condition, which is the most common situation in experimental metrology of large deformation. The BS strategy can also be used for non-monotonic loading experiments with minor modification. For instance, in combination with loading data, the loading process could be divided into several monotonic loading subsections, and then the BS strategy could be applied. Another limitation of the BS strategy is that it inherently requires that all the data are available at the start of the analysis; e.g., the calculation should be offline. This requirement should not be a significant limitation in practice since most DIC analysis is offline due to the computation burden.

5. CONCLUSION

In this research, the BS strategy is proposed to solve the problem of selecting proper reference frames in varying situations. The key idea of this strategy is reducing the frame step into one half when the correlation failed.

The effectiveness of the BS strategy was compared with the CS strategy on two simulated experiments. The BS strategy successfully tracked the POIs to the last frame. In contrast, the CS strategies failed in the cases of the largest frame step. The BS strategy also automatically reduced the frame step in the period of the high rotation rate in the first experiment and large speckle replacement rate in the second experiment. The RMSE calculated by the BS strategy was also lower than the results of all CS strategies. The computation efficiency of the BS strategy was on the same level of most CS strategies and lower than the CS strategy with larger frame step. The moderate computation time of the BS strategy is worthy for the higher convergence and accuracy, and it avoids the time-consuming process of manual selection of the frame step in the CS strategy.

The robustness of the BS strategy was also demonstrated in the real-world experiment. It successfully tracked all POIs including the necking region with large plastic deformation above 70% of the engineering strain. The determined frame step was automatically reduced in the period of higher loading rate and the necking.

ACKNOWLEDGEMENT

Funding: This study was funded by NASA EPSCoR (NNX13AM99A), National Science Foundation (CMMI-1625736), DOE STTR (DESC0018879), and the Intelligent Systems Center (ISC) and Material Research Center at Missouri S&T.

REFERENCES

[1] Blaber, J., Adair, B., and Antoniou, A., 'Ncorr: open-source 2d digital image correlation matlab software,' Experimental Mechanics, 2015, **55**(6), pp. 1105–1122.

[2] Chen, Z., Shao, X., Xu, X., and He, X., 'Optimized digital speckle patterns for digital image correlation by consideration of both accuracy and efficiency,' Applied optics, 2018, **57**(4), pp. 884–893.

[3] Chi, Y. and Pan, B., 'Spatial-temporal subset-based digital image correlation: A general framework,' CoRR, 2018, **abs/1812.04826**.

[4] Goh, C., Ismail, H., Yen, K., and Ratnam, M., 'Single-step scanner-based digital image correlation (sb-dic) method for large deformation mapping in rubber,' Optics and Lasers in Engineering, 2017, **88**, pp. 167–177.

[5] Matthews, L., Ishikawa, T., and Baker, S., 'The template update problem,' IEEE transactions on pattern analysis and machine intelligence, 2004, **26**(6), pp. 810–815.

[6] Pan, B., 'Reliability-guided digital image correlation for image deformation measurement,' Applied optics, 2009, **48**(8), pp. 1535–1542.

[7] Pan, B., 'Recent progress in digital image correlation,' Experimental Mechanics, 2011, **51**(7), pp. 1223–1235.

[8] Pan, B., 'An evaluation of convergence criteria for digital image correlation using inverse compositional gauss–newton algorithm,' Strain, 2014, **50**(1), pp. 48–56.

[9] Pan, B., 'Digital image correlation for surface deformation measurement: historical developments, recent advances and future goals,' Measurement Science and Technology, 2018, **29**(8), p. 082001.

[10] Pan, B., Dafang, W., and Yong, X., 'Incremental calculation for large deformation measurement using reliability-guided digital image correlation,' Optics and Lasers in Engineering, 2012, **50**(4), pp. 586–592.

[11] Pan, B., Li, K., and Tong, W., 'Fast, robust and accurate digital image correlation calculation without redundant computations,' Experimental Mechanics, 2013, **53**(7), pp. 1277–1289.

[12] Pan, B., Qian, K., Xie, H., and Asundi, A., 'Two-dimensional digital image correlation for in-plane displacement and strain measurement: a review,' Measurement science and technology, 2009, **20**(6), p. 062001.

[13] Su, Y., Zhang, Q., Fang, Z., Wang, Y., Liu, Y., and Wu, S., 'Elimination of systematic error in digital image correlation caused by intensity interpolation by introducing position randomness to subset points,' Optics and Lasers in Engineering, 2019, **114**, pp. 60–75.

[14] Sur, F., Blaysat, B., and Grediac, M., 'Rendering deformed speckle images with a boolean model,' Journal of Mathematical Imaging and Vision, 2017, pp. 1–17.

[15] Tang, Z., Liang, J., Xiao, Z., and Guo, C., 'Large deformation measurement scheme for 3d digital image correlation method,' Optics and Lasers in Engineering, 2012, **50**(2), pp. 122–130.

[16] Zhang, Y., Xie, X., Wang, X., Li, Y., and Ling, X., 'Adaptive image mismatch removal with vector field interpolation based on improved regularization and gaussian kernel function,' IEEE Access, 2018, **6**, pp. 55599–55613, ISSN 2169-3536, doi: 10.1109/ACCESS.2018.2871743.

[17] Zhang, Y., Yan, L., and Liou, F., 'Improved initial guess with semi-subpixel level accuracy in digital image correlation by feature-based method,' Optics and Lasers in Engineering, 2018, **104**, pp. 149–158.

[18] Zhou, Y., Sun, C., and Chen, J., 'Adaptive subset offset for systematic error reduction in incremental digital image correlation,' Optics and Lasers in Engineering, 2014, **55**, pp. 5–11.

III. DETERMINATION OF CONSTITUTIVE RELATION FROM MINIATURE TENSILE TEST WITH DIGITAL IMAGE CORRELATION

Yunlu Zhang

Department of Mechanical & Aerospace Engineering

Missouri University of Science and Technology

Rolla, Missouri 65409–0050

Email: yzdyf@mst.edu

ABSTRACT

Determination of constitutive relation from the miniature tensile test is of high interest in multiple areas. Here a convenient experimental method to determine the true stress-strain curve from miniature tensile test is proposed. The instantaneous cross-section area is estimated by only one camera in aid of digital image correlation (DIC) technique. This method is applied to a commercial pure Titanium (CPTi) and Aluminum 6061 alloy (Al6061) for both miniature and standard size specimens. The results show that the extracted true stress-strain curves are highly matched for different dimensions. The correctness of the true stress-strain curve was evaluated by the finite element analysis (FEA) method. Finally, the constitutive behavior of additive manufactured and wrought stainless steel 304L (SS304) was also determined by the proposed method.

Keywords: constitutive relation, digital image correlation, tensile test

1. INTRODUCTION

Recently, researchers have shown an increasing interest in the mechanical test of miniature specimens and acquiring the relevant properties. The use of miniature specimens could provide several advantages and avoid a few limitations in comparison with

conventional specimens. First, the microscale mechanics of material and performance of microcomponents could be directly studied [7]. It is also a valuable tool for evaluating the local properties of inhomogeneous materials like weldment [16] and functional gradient material [10]. Another big motivation comes from the limited volume of the investigated material. To semi-nondestructively evaluate the mechanical properties of the in-service component, the size and shape of available material are much restricted. The nuclear research community also prefers the miniature specimen to reduce the radiological dose from the activated material and efficiently use of costly reactor space [4, 5, 6, 13].

The tensile test is the most fundamental and widely used technique to obtain the strength and ductility properties and stress-strain behavior of materials. Therefore, the miniature tensile test is widely studied. However, in contrast to the standard tensile specimen specified in ASTM E8 or ISO 6892, many different designs of miniature tensile specimens have been proposed [2, 5, 6, 13, 14, 15, 21, 27]. They feature different dimensions of the gauge section, aspect ratio of the cross-section, radius of the fillet, and gripping mechanism. One conclusion could be drawn from the results of various miniature tensile tests, the determined yield strength, ultimate strength, and uniform elongation are comparable to the standard specimen results. Chen *et al.* [2] concluded that the yield strength of the CuAl7 alloy decreased with increasing thickness then stabilized when the thickness was larger than 0.5 mm. The yield strength is nearly constant when the ratio of thickness t to grain size d is larger than a critical value (about 21). This is coincident with [15], in which the critical ratio was 16, 3.4 and 1.5 for 20MnMoNi55, CrMoV and SS304LN, respectively.

Most mentioned miniature tensile research focused on the properties of yield strength, ultimate strength, uniform elongation, and ultimate elongation, the true constitutive relation was seldom considered. Gussev *et al.* [5] mentioned that the true stress-strain curves describing strain-hardening behavior were very close for different types of specimens. However, these true stress-strain curves were only calculated till the ultimate stress, e.g., the end of uniform deformation. The true constitutive relation at large strain is im-

portant in plastic analysis and large deformation simulation. The true stress-strain curve represents the deformation of the yield surface in the stress space. While the engineering stress-strain curve determined from the ordinary uniaxial tensile test is extensively used for characterizing plastic hardening behavior of metals, the result becomes invalid after the maximum load or the onset of necking due to the nonuniform deformation and triaxial stress state. More complicated measurement and analysis need to be applied to get the true constitutive relation at large strain.

In general, two types of approaches have been widely studied to derive the constitutive relation. The first approach is the correction method initially developed by Bridgman [1] in the 1950s. This method relies on the continuous measurement of the area of cross-section and the radius of curvature in the neck of the cylindrical specimen. The true axial stress is first calculated based on the instantaneous area of the cross-section, then it is multiplied by a correction factor to yield the equivalent stress. The analytical correction factor is based on a few assumptions. Later, Le Roy *et al.* [17] proposed a simplified equation to calculate the correction factor that eliminates the requirement of the radius of curvature. The correction method has been extended to specimens with rectangle cross-section by Choung and Cho [3], Scheider *et al.* [22], Zhang *et al.* [26]. These analyses were based on FEA simulation since an analytical solution for specimens with rectangle cross-section is hard to get. In order to measure the instantaneous area of the cross-section, interrupted tests were possible but burdensome [3]. To overcome this limitation, the non-contact optical metrology method digital image correlation (DIC) was applied to continuously measure the area of the cross-section without interruption for cylindrical [28] and rectangle [23] specimens. However, complex mirrors or multiple cameras are required for these DIC setups.

Another type of approach is the inverse FEA method, which iteratively adjusts the true stress-strain curve in the FEA simulation to match the experimental measured quantities such as virtual work [11], load force [8, 18], or axial stress [9]. The advantage of the inverse

FEA method is that the description of the true stress-strain curve could be the piece-wise linear function instead of the predefined model. However, the limitation is that the iterative process is laborious and time-consuming.

The objective of current research is to provide a simple method to determine the constitutive behavior of material up to the onset of localized necking by miniature tensile test and DIC. Only one camera with the telecentric is required in the DIC setup that provides the accurate and continuous measurement of the cross-section area. The correction method is used in this research for its simplicity. Overall, the proposed method is easy to be applied in the real application.

The specimen design and experimental setup are first described in Section 2. The detail of the proposed method is discussed in Section 3. The extracted true stress-strain curves from the standard and miniature specimens by the new method are compared in Section 4. The correctness of the derived true stress-strain curve is further evaluated by FEA simulation in Section 5. The proposed method is then applied to the selective laser melting (SLM) material in Section 6. Finally, the conclusion is given in Section 7.

2. EXPERIMENT

Miniature and ASTM tensile specimens of two types of materials were manufactured and tested to compare the extracted true tress-strain curves. The details of the (i) materials, (ii) specimens, and (iii) experiment setup are presented in subsequent subsections.

2.1. MATERIALS

Two types of materials were tested to compare the extracted true tress-strain curves. Commercial pure grade 2 Titanium (CP-Ti) and Aluminum 6061-T6 (Al6061) were selected in this study for their different strength and hardening behavior. In addition, Al6061 is of special interest in nuclear structural material [12]. The chemical composition provided

by the supplier (McMaster-Carr, Il, USA) is listed in Table 1. The grain distribution of CP-Ti and Al6061 were revealed by KellerâĂŹs reagent and Weck's reagent respectively, and the optical microscope images are shown in Figure 1. The average grain size of CP-Ti and Al6061 is about 10 and 40 um respectively. No heat treatment has been done for the received materials.

Table 1. Element composition of the investigated materials.

Material	Composition, wt%
Al6061	Al: 97.41, Si: 0.77, Fe: 0.39, Cu: 0.30, Mn: 0.10
	Mg: 0.85, Cr: 0.10, Zn: 0.05, Ti: 0.03, Other: 0.15
CP-Ti	C: 0.05, N: 0.03, O: 0.25, Fe: 0.30, H:0.015, Ti: Bal.

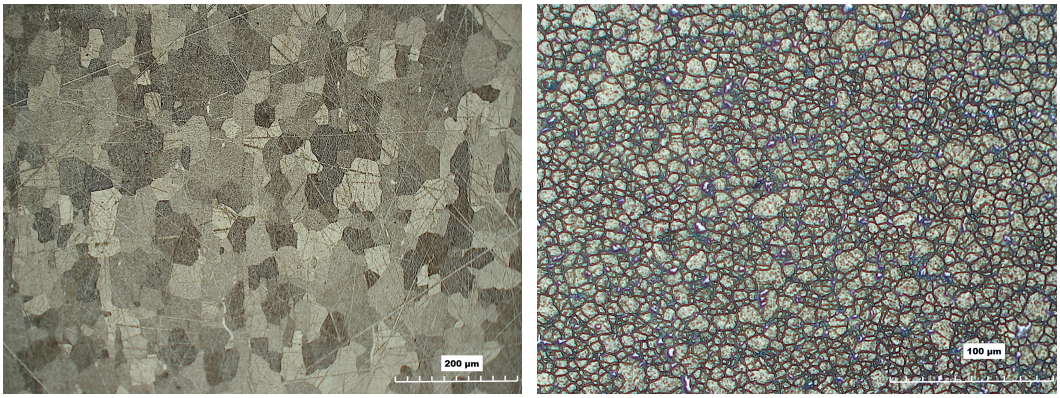

(a) CP-Ti (b) Al6061

Figure 1. Optical microscope images of the raw materials.

2.2. SPECIMENS

The miniature specimen with the gauge section nominal dimension of $3 \times 1 \times 1$ mm termed MT2 was adopted in this investigation. This design was also used in [10]. To compare the results of standard tensile specimens, the smallest rectangle specimen defined in ASTM E8 standard, the ASTM subsize specimen with the gauge length of 25 mm, was

also used here. Figure 2 (a) and (b) show the geometry and dimension of the MT2 and ASTM specimen. Figure 2 (c) is a visual representation of the huge size difference between these tensile specimens.

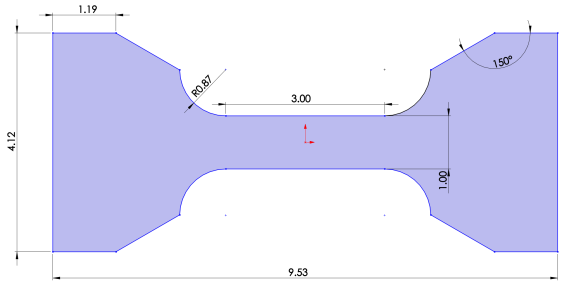

(a) MT2

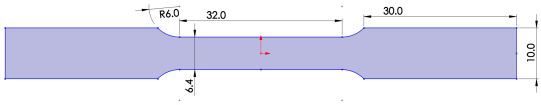

(b) ASTM

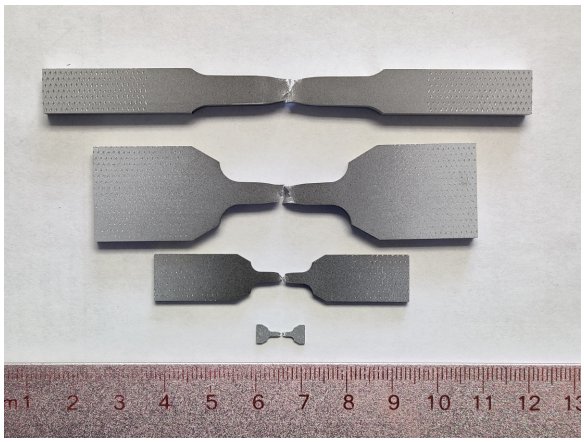

(c) Size comparison

Figure 2. Shape and dimension in mm of the (a) MT2, (b) ASTM specimen, and (c) size comparison of ASTM, MT2-5, MT2-2.5, and MT2 specimens (top to bottom).

The thickness of the MT2 specimen was set to 1 mm. This specific thickness serves a few purposes. First, the 1:1 width-to-thickness ratio enables the estimation of cross-section area by only one camera. The ratio of the thickness reduction is assumed to be the same as the ratio of the width reduction that is directly measured. Second, 1 mm thickness is large enough for most metal materials with typical grain sizes to fulfill the ratio of thickness

to grain size requirement [2]. Finally, the 1:1 width-to-thickness ratio was studied in [3] to derive the correction equation, so the results could be directly applied. The low aspect ratio also minimizes the strain gradient in the cross-section of the neck [3]. The thickness of ASTM subsize specimen is not specified in the ASTM E8 standard. In order to get comparable results, it was set to 6 mm to get the 1:1 width-to-thickness ratio.

To study the effect of the size of the miniature specimen, 2.5 and 5 times proportionally scaled MT2 specimens were machined for Al6061. The gripping area of the scaled up specimens were extended to fit the wedge grip as shown in Figure 2 (c). Hereinafter four types of Al6061 specimens are termed Al6061-MT2, Al6061-MT2-2.5, Al6061-MT2-5, and Al6061-ASTM. Similarly, two types of CP-Ti specimens are termed CPTi-MT2 and CPTi-ASTM.

The MT2 specimens were cut to the specified dimensions by electro-discharge machining and then grounded with 1200-grit SiC abrasive paper. Other specimens were machined to the specified dimensions without surface treatment. The surface of the specimen was coated by the white and black paint sequentially to create the contrast speckle pattern by airbrushing.

2.3. EXPERIMENT SETUP

A customized shoulder grip was manufactured to facilitate the test of MT2 specimens on the Instron 5969 universal test machine (Instron, MA, USA). In order to minimize the torsion and bending on the specimen, the grip is designed to be self-aligned by 2 perpendicular joints. For other types of specimens, the ordinary wedge grip was used. Figure 3 shows the experiment setup of the two types of grips for MT2 and ASTM specimens. For all the specimens, the constant cross-head speed control was used with target nominal strain rate of 0.003 /s.

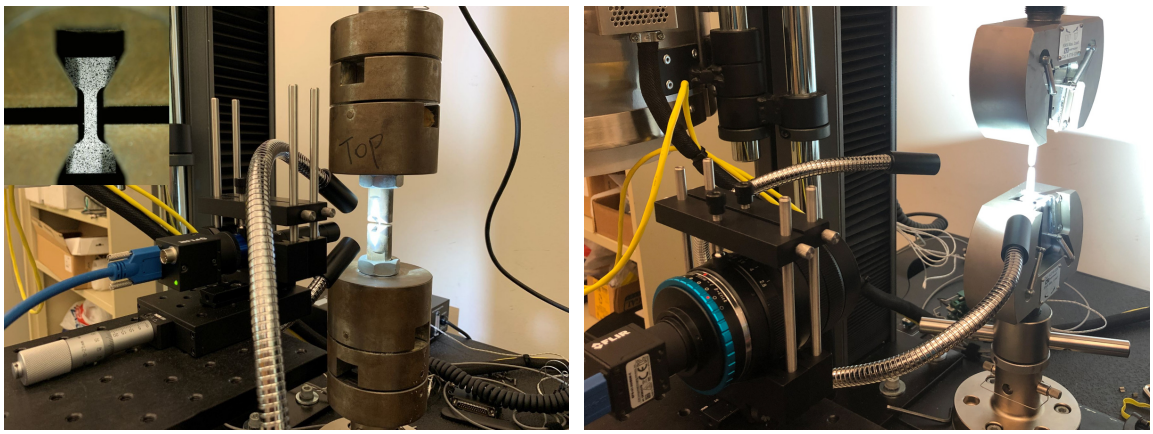

(a) MT2 (b) ASTM

Figure 3. Experiment setup of the (a) MT2 and (b) ASTM specimen. The inset of (a) shows the MT2 specimen in the shoulder grip.

During the tensile test, the out-of-plane motion of the gauge section is unavoidable due to the rotation of the specimen or the Poisson effect. The shallow depth of field associated with the high magnification and smaller object distance makes this problem more severe for the MT2 specimen. Therefore, a telecentric (RT-HR-1M-71, Opto Engineering, TX, USA) lens was adopted to eliminate the out-of-plane effect of MT2 specimens. The compatible camera (BFS-U3-50S5M-C, FLIR Systems, OR, USA) was chosen for its high resolution and large sensor size. Other specimens were recorded by a 60mm macro lens (Laowa 60mm f/2.8 2X Ultra-Macro, Anhui, China) and 1" sensor size camera (BFS-U3-200S6M-C, FLIR Systems, OR, USA). The specimens were illuminated by high-intensity white LED light. The images were captured at a constant frame rate of 8 frames per second. The number of repetition for the MT2 specimens and other types of specimens was 10 and 3 respectively.The fracture surfaces of the tested specimens were observed by the ASPEX-PICA 1020 scanning electron microscope (Aspex Corporation, PA, USA).

3. METHOD TO DETERMINE TRUE STRESS-STRAIN CURVE

The directly measured data from the tensile test was the load data F from the load cell. The engineering stress S is determined from the initial area of the cross-section A_0

$$S = F/A_0 \tag{1}$$

The displacement and strain were measured from the DIC analysis of recorded images of the deformation process. Here the key measurement was the minimum neck width w_{neck}. The points of interest (POIs) corresponding two ends of the neck were identified at the last frame before the fracture happened as shown in Figure 4(a). There were a few (typical 5) closely aggregated POIs on each side of the neck. Neck width w_{neck} was calculated from the distance between the centroids of two groups of POIs to minimum the random error.

These POIs were tracked from the end to the start of the recorded images to obtain the instantaneous w_{neck} during the test. Due to the large ductile strain in the neck, the regular DIC algorithm could not find the correct correspondence in the first frame from the last frame. The bisection search method that could automatically adjust the frame step was used to overcome this difficulty [24]. The feature matching method [25] and inverse compositional Gauss-Newton method [20] were the initial searching and subpixel searching algorithm respectively. The subset size for every POI was 21×21 px.

Equivalent true strain ϵ_{eq} and average true axial strain can be estimated from the width reduction

$$\epsilon_{eq} = \epsilon_a = \ln(A_0/A) = 2\ln(w_0/w_{neck}) \tag{2}$$

where w_0 is the initial neck width. Here the first sign of equality comes from the assumption of incompressibility and neglected elastic strain, and the third sign of equality is based on the equal percentage of reduction in the thickness and width direction, which is valid in the current implementation due to the aspect ratio of 1:1. Figure 4(b) shows the derived width reduction and equivalent true strain.

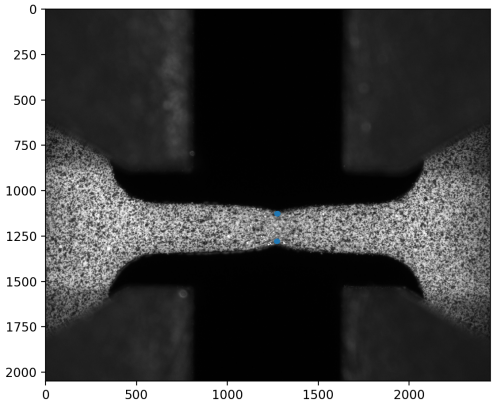

(a)

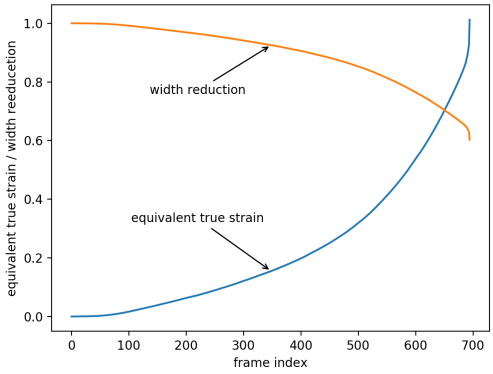

(b)

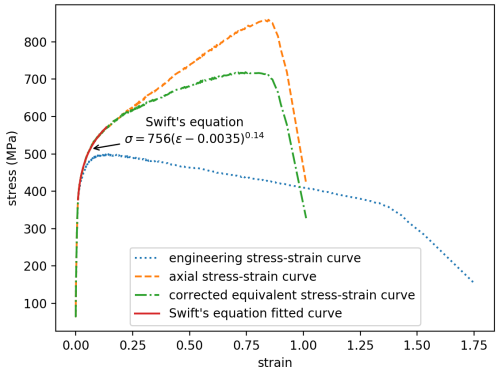

(c)

Figure 4. The process of deriving true stress-strain curve of a CPTi-MT2 specimen. (a) Identified two ends of the neck, (b) width reduction determined from the neck deformation and derived equivalent strain, and (c) engineering stress-strain curve, axial stress-strain curve, determined hardening exponent n, and corrected equivalent stress-strain curve.

The axial true stress can be estimated from the instantaneous cross-section area A

$$\sigma_a = \frac{F}{A} = S\frac{A_0}{A} = S\left(\frac{w_0}{w_{neck}}\right)^2 \tag{3}$$

The correction method [3] is adopted here to obtain equivalent stress σ_{eq} from the axial true stress σ_a

$$\sigma_{eq} = \sigma_a \xi(\epsilon_{eq}) \tag{4}$$

where the correction parameter $\xi(\epsilon_{eq})$ is a function of the hardening exponent n and σ_{eq}

$$\xi(\epsilon_{eq}) = \begin{cases} 1 & \epsilon_{eq} \leq 1.4n \\ \alpha\epsilon_{eq}^2 + \beta\epsilon_{eq} + \gamma & \epsilon_{eq} > 1.4n \end{cases} \tag{5}$$

where $\alpha = -0.0704n - 0.0275$, $\beta = 0.4550n - 0.2926$, and $\gamma = 0.1592n + 1.024$.

The hardening exponent n is determined from fitting the Swift's equation

$$\sigma = K(\epsilon + \epsilon_0)^n \tag{6}$$

to the region between the yielding point and maximum load point of the axial true stress-strain curve.

Figure 4(c) demonstrates the process of extracting the true stress-strain curve of a CPTi-MT2 specimen. In this figure, the engineering stress is determined by equation 1. The engineering strain is calculated from

$$\epsilon_{eng} = \frac{L - L_0}{L_0} = \frac{A_0}{A} - 1 = \left(\frac{w_0}{w_{neck}}\right)^2 - 1 \tag{7}$$

where L and L_0 are the instantaneous and initial length of the gauge section respectively.

4. RESULTS

Figure 5 shows the derived equivalent stress-strain curves and engineering stress-strain curves for the different alloys and dimensions. The true stress-strain curves were cropped to the maximum points since the strain softening was not considered here. The stress drop in the full true stress-strain curve may be attributed to the invalidity of diffused necking assumption due to the start of localized necking.

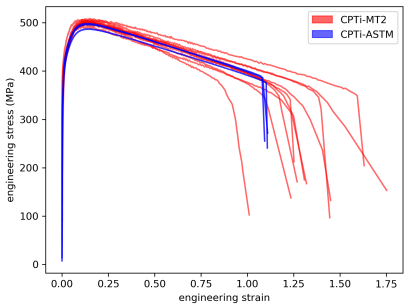

(a) CPTi engineering stress-strain curve

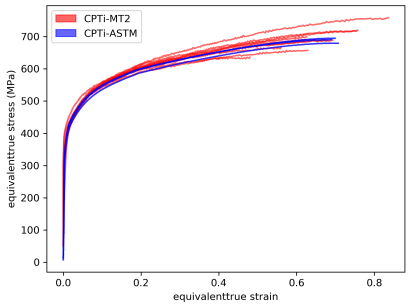

(b) CPTi equivalent true stress-strain curve

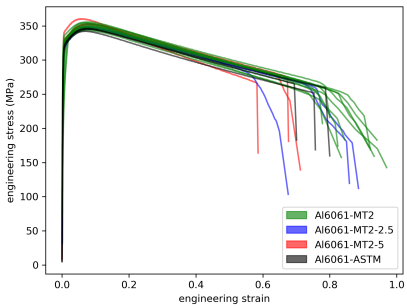

(c) Al6061 engineering stress-strain curve

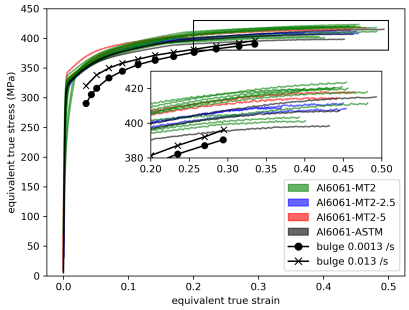

(d) Al6061 equivalent true stress-strain curve

Figure 5. Derived true stress-strain and engineering stress-strain curves of CPTi and Al6061 specimens. The results of bulge tests in (d) are from [19].

The different dimensions did not lead to a significant difference in the derived engineering stress-strain curve of Al6061. The average total elongation of Al6061-MT2 specimens is larger than the rest types of specimens, e.g., reduce the gauge length will

increase the apparent total elongation. This observation agrees with literature [5, 27]. For CPTi specimens, the trend is the same. Larger scatters appear in the engineering stress-strain curves of MT2 specimens after the strain value of 0.8.

Table 2. Comparison of mechanical parameters determined from miniature and ASTM specimens of CPTi and Al6061.

	CPTi-ASTM	CPTi-MT2	Al6061-ASTM	Al6061-MT2-5	Al6061-MT2-2.5	Al6061-MT2
strength coefficient K (MPa)	737 ± 6	759 ± 17	479 ± 8	482 ± 6	458 ± 3	482 ± 28
hardening exponent n	0.132 ± 0.002	0.140 ± 0.010	0.104 ± 0.007	0.094 ± 0.003	0.079 ± 0.003	0.102 ± 0.028
yielding stress (0.2%) S_y (MPa)	348 ± 5	352 ± 21	313 ± 2	318 ± 10	300 ± 2	305 ± 11
ultimate stress S_u (MPa)	494 ± 5	502 ± 5	345 ± 2	355 ± 4	347 ± 1	338 ± 6

The true stress-strain curves of different types of specimens are close for both materials. The larger variation of the results of MT2 specimens may come from the local ununiformity of the composition or defect in respect to the smaller gauge section. However, the average true stress-strain curves of different types are in excellent agreement, which indicates the variation can be reduced by averaging.

The true stress-strain curve of Al6061 determined by the bulge test [19] is also plotted in 5 (d) for comparison. The result from the bulge test is not accurate at the initial stage since the assumption of perfect spherical bulge shape is not valid. Therefore some differences exist between these two approaches. However, at the later stage of the true stress-strain curve, the results are more close as shown in the inset of 5 (d). It should also be noted that the range of the strain determined by the current method is larger than the bulge test.

The yielding stress S_y, ultimate stress S_u, strength coefficient K, and hardening exponent n determined from the engineering stress-strain curve and true stress-strain curve respectively are listed in Table 2. The average derived properties also show no dimension dependence. The 1-5% difference complies with the literature [21]. The standard deviation of the MT2 specimens is typically larger than the ASTM specimen, which may attribute to the discussed local variation effect.

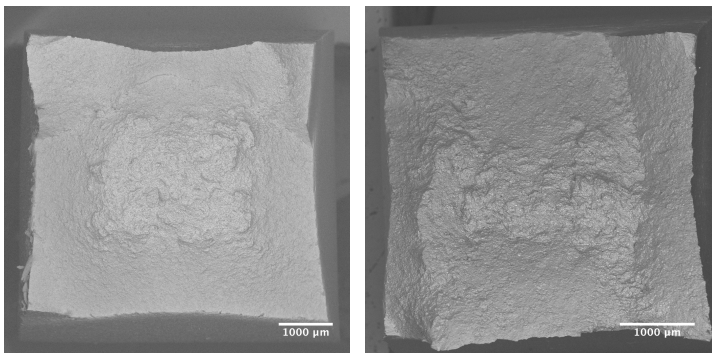

(a) Al6061-ASTM (b) Al6061-MT2-5

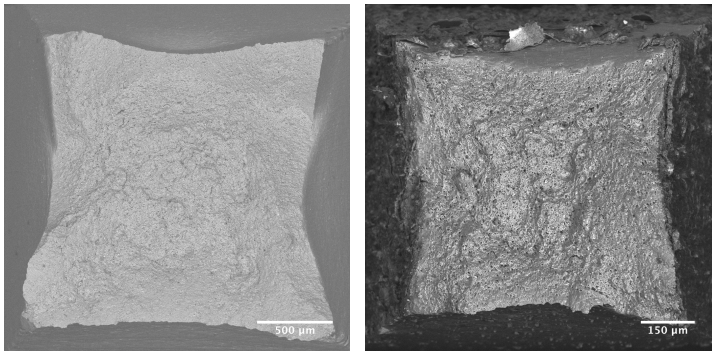

(c) Al6061-MT2-2.5 (d) Al6061-MT2

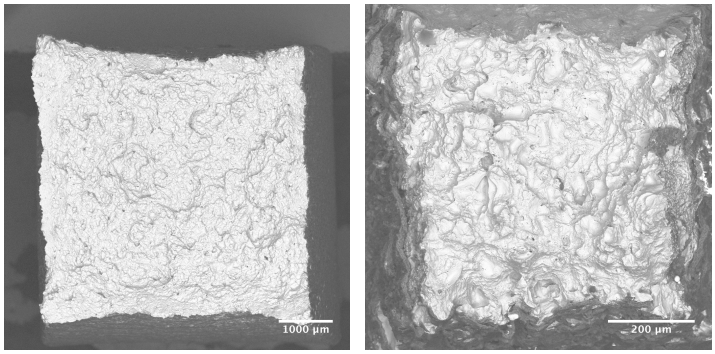

(e) CPTi-ASTM (f) CPTi-MT2

Figure 6. Fracture surface of tested specimens. The image plane was perpendicular to the load axis.

The fracture surfaces of tested specimens are shown in Figure 6. The center of the specimen retracts more than the corner, e.g., the cushioning effect is evident [3]. The aspect ration of the fracture specimen is close to 1 that indicates the assumption of equal reduction in thickness and width direction is valid for the current implementation.

5. FEA EVALUATION

The correctness of the derived true stress-strain curve was evaluated by the FEA simulation. The experimental and simulated load vs. equivalent strain curves were compared. Ideally, the load vs. extension curve should be used in the comparison, because these two quantities are directly measured from the experiment. However, due to the deformation of the grip and loading frame, the measured extension will always be larger than the calculated displacement. Therefore, the equivalent strain was used to represent the degree of deformation for both DIC and FEA results, and they were calculated based on Eq. 2.

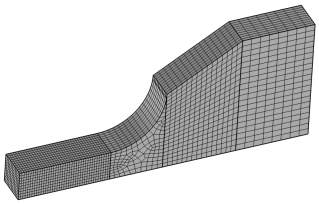

(a) MT2

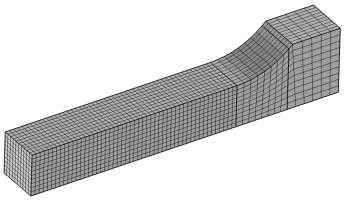

(b) ASTM

Figure 7. FEA mesh of the (a) MT2 and (b) ASTM specimen.

The commercial software COMSOL Multiphysics® was used to perform the simulation. One-eighth of the full specimen was model to take advantage of the symmetry. The generated secondary order meshes are shown in Figure 7. The size of the cubic element in the gauge section was 50 um and 320 um respectively. The prescribed displacement boundary condition was applied on the shoulder face of the MT2 model. For the ASTM model, only a portion of the gripping section was considered to reduce the computation cost. The

prescribed displacement was applied on the cut cross-section. The width in the center of the gauge section was gradually reduced to 99.5% of the actual dimension to trigger the start of necking.

The material model was assumed to be isotropic hardening, and the von Mises stress yield criterion was used. The yielding stress and the flow curve were directly adopted from the previous results without smoothing. The elastic properties (Young's modulus and Poisson's ratio) were the nominal values. The load curve of a random specimen from each type was chosen to be compared with FEA result.

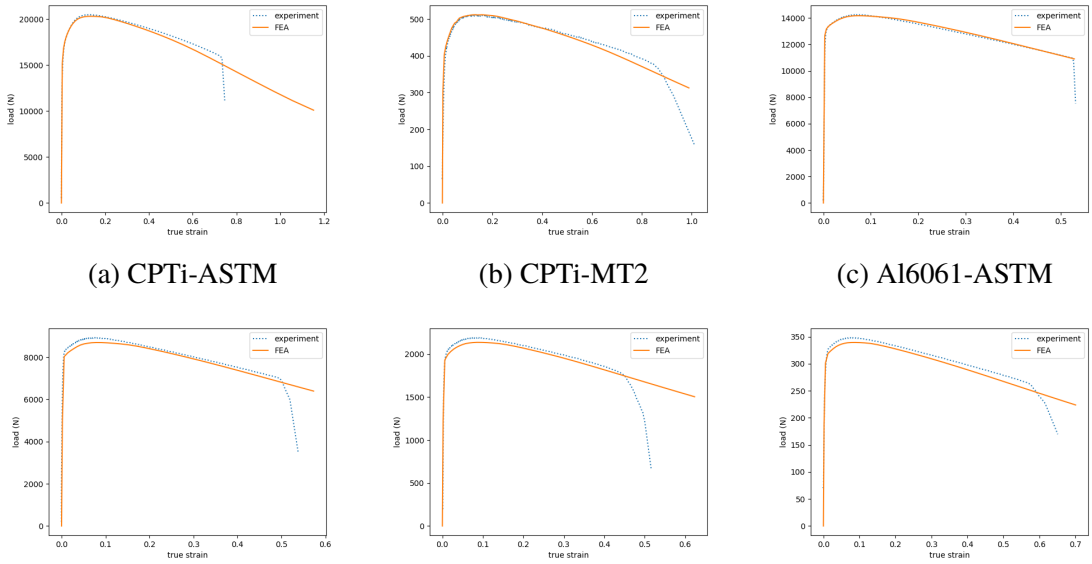

(a) CPTi-ASTM (b) CPTi-MT2 (c) Al6061-ASTM

(d) Al6061-MT2-5 (e) Al6061-MT2-2.5 (f) Al6061-MT2

Figure 8. Comparison of the load vs. equivalent strain curves from the experiment and FEA simulation.

Figure 8 shows the load vs. equivalent strain curves from the experiment and FEA simulation. The reaction load of FEA simulation was calculated on the face that the displacement condition applied. The simulated load response is close to the experiment results before and after the maximum load, and only deviates at the end of the test. The deviation may be attributed to the start of the localized necking that violates the uniform

necking assumption. The maximum deviation of the load is about 2-3% before the localized necking. The well-matched results indicate the derived true stress-strain curve is capable to represent the constitutive behavior of the tested materials.

6. APPLICATION IN SS304

The proposed method was applied to determine the constitutive property of the SLM stainless steel 304L (SS304) part. The direction of the tensile load was perpendicular to the build direction. The build parameters were: power 200 W, hatch space 85 um, scan speed 0.8 m/s, layer thickness 50 um. SS304L in the wrought annealed state was also included for comparison. The specimens were prepared by the same method described in Section 2.2. The number of repetition for each type of material was 5.

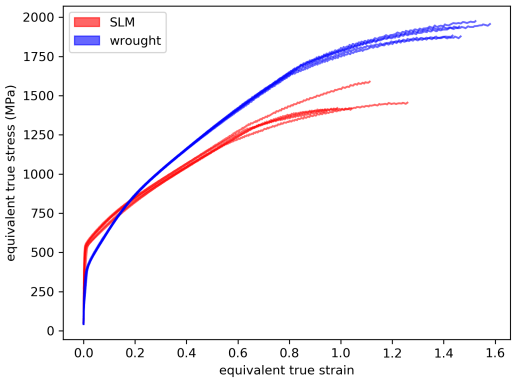

Figure 9. Derived true stress-strain curves of SLM and wrought SS304.

Table 3. Comparison of mechanical parameters determined from SLM and wrought SS304 specimens.

	SLM	wrought
strength coefficient K (MPa)	1399 ± 20	1744 ± 6
hardening exponent n	0.41 ± 0.02	0.48 ± 0.01
yielding stress (0.2%) S_y (MPa)	474 ± 48	362 ± 31
ultimate stress S_u (MPa)	707 ± 7	784 ± 2

The determined true stress-strain curves are shown in Figure 9. Good repeatability achieved for each type of material. The SLM SS304 exhibits the higher yielding stress but lower plastic hardenability than the wrought state. The determined strength coefficient K and hardening exponent n are shown in Table 3 also confirm this trend. The difference in constitutive relations can be attributed to the faster cooling rate during SLM process.

7. CONCLUSION

This study demonstrates the feasibility to extract material constitutive behavior by a simple miniature tensile test. The following conclusions were obtained.

1. A new miniature tensile specimen with a parallel section of $3 \times 1 \times 1$ mm was used. The 1:1 width-to-thickness ratio enables the estimation of cross-section area by only one camera, and the telecentric lens can eliminate the effect of out-of-plane motion.

2. The derived true stress-strain curves and mechanical parameters of Al6061 and CPTi from miniature specimens match well with the results of standard specimens. No dimension dependence has been observed in the results.

3. FEA simulation was used to evaluate the correctness of the derived true stress-strain curve. The maximum deviation of the simulated and experimental load is only 2-3%. The result shows that the derived true stress-strain curve is capable to represent the constitutive behavior of the tested materials.

The current study assumes that the material is isotropic, e.g., anisotropic hardening is not considered. In the future, it can be investigated by multiple cameras with modified correction equations so that more types of material can be studied.

ACKNOWLEDGEMENT

Funding: This study was funded by NASA EPSCoR (NNX13AM99A), National Science Foundation (CMMI-1625736), DOE STTR (DESC0018879), and the Intelligent Systems Center (ISC) and Material Research Center at Missouri S&T.

REFERENCES

[1] Bridgman, P. W., *Studies in large plastic flow and fracture*, volume 177, McGraw-Hill New York, 1952.

[2] Chen, F., Chen, S., Dong, X., Li, C., Hong, X., and Zhang, X., 'Size effects on tensile strength of aluminum–bronze alloy at room temperature,' Materials & Design, 2015, **85**, pp. 778–784.

[3] Choung, J. and Cho, S., 'Study on true stress correction from tensile tests,' Journal of Mechanical Science and Technology, 2008, **22**(6), pp. 1039–1051.

[4] Geringer, J. and Katoh, Y., 'Atf neutron irradiation program technical plan,' Technical report, Oak Ridge National Lab.(ORNL), 2016.

[5] Gussev, M., Busby, J., Field, K., Sokolov, M., and Gray, S., 'Role of scale factor during tensile testing of small specimens,' in 'Small Specimen Test Techniques: 6th Volume,' ASTM International, 2015.

[6] Gussev, M. N., Howard, R. H., Terrani, K. A., and Field, K. G., 'Sub-size tensile specimen design for in-reactor irradiation and post-irradiation testing,' Nuclear Engineering and Design, 2017, **320**, pp. 298–308.

[7] Jaya, N. B. and Alam, M. Z., 'Small-scale mechanical testing of materials,' Current Science, 2013, **105**(8), pp. 1073–1099.

[8] Kamaya, M. and Kawakubo, M., 'True stress–strain curves of cold worked stainless steel over a large range of strains,' Journal of Nuclear Materials, 2014, **451**(1-3), pp. 264–275.

[9] Kamaya, M., Kitsunai, Y., and Koshiishi, M., 'True stress–strain curve acquisition for irradiated stainless steel including the range exceeding necking strain,' Journal of Nuclear Materials, 2015, **465**, pp. 316–325.

[10] Karnati, S., Zhang, Y., Liou, F. F., and Newkirk, J. W., 'On the feasibility of tailoring copper–nickel functionally graded materials fabricated through laser metal deposition,' Metals, 2019, **9**(3), p. 287.

[11] Kim, J.-H., Serpantié, A., Barlat, F., Pierron, F., and Lee, M.-G., 'Characterization of the post-necking strain hardening behavior using the virtual fields method,' International Journal of Solids and Structures, 2013, **50**(24), pp. 3829–3842.

[12] Kim, Y. S., Hofman, G., Robinson, A., Snelgrove, J., and Hanan, N., 'Oxidation of aluminum alloy cladding for research and test reactor fuel,' Journal of Nuclear Materials, 2008, **378**(2), pp. 220–228.

[13] Kohno, Y., Kohyama, A., Hamilton, M. L., Hirose, T., Katoh, Y., and Garner, F. A., 'Specimen size effects on the tensile properties of jpca and jfms,' Journal of nuclear materials, 2000, **283**, pp. 1014–1017.

[14] Kumar, K., Pooleery, A., Madhusoodanan, K., Singh, R., Chakravartty, J., Dutta, B., and Sinha, R., 'Use of miniature tensile specimen for measurement of mechanical properties,' Procedia Engineering, 2014, **86**, pp. 899–909.

[15] Kumar, K., Pooleery, A., Madhusoodanan, K., Singh, R., Chatterjee, A., Dutta, B., and Sinha, R., 'Optimisation of thickness of miniature tensile specimens for evaluation of mechanical properties,' Materials Science and Engineering: A, 2016, **675**, pp. 32–43.

[16] LaVan, D., 'Microtensile properties of weld metal,' Experimental techniques, 1999, **23**(3), pp. 31–34.

[17] Le Roy, G., Embury, J., Edwards, G., and Ashby, M., 'A model of ductile fracture based on the nucleation and growth of voids,' Acta Metallurgica, 1981, **29**(8), pp. 1509–1522.

[18] Liu, H., Shen, Y., Yang, S., Zheng, P., and Zhang, L., 'A comprehensive solution to miniaturized tensile testing: Specimen geometry optimization and extraction of constitutive behaviors using inverse fem procedure,' Fusion Engineering and Design, 2017, **121**, pp. 188–197.

[19] Mahabunphachai, S. and Koç, M., 'Investigations on forming of aluminum 5052 and 6061 sheet alloys at warm temperatures,' Materials & Design (1980-2015), 2010, **31**(5), pp. 2422–2434.

[20] Pan, B., Li, K., and Tong, W., 'Fast, robust and accurate digital image correlation calculation without redundant computations,' Experimental Mechanics, 2013, **53**(7), pp. 1277–1289.

[21] Ramchandran, D., Kumar, A., Chaitanya, G., Karthik, V., and Kolhatkar, A., 'Development and validation of a miniature tensile specimen for determination of mechanical properties,' Journal of Testing and Evaluation, 2019, **47**(5).

[22] Scheider, I., Brocks, W., and Cornec, A., 'Procedure for the determination of true stress-strain curves from tensile tests with rectangular cross-section specimens,' Journal of engineering materials and technology, 2004, **126**(1), pp. 70–76.

[23] Yazzie, K., Williams, J., and Chawla, N., 'Quantifying necking of rectangular tensile specimens using a mirror-based image analysis system,' Materials Letters, 2012, **74**, pp. 243–246.

[24] Zhang, Y., Yan, L., Karnati, S., and Liou, F., 'Bisection searching based reference frame update strategy for digital image correlation,' SN Applied Sciences, 2019, **1**(6), p. 588.

[25] Zhang, Y., Yan, L., and Liou, F., 'Improved initial guess with semi-subpixel level accuracy in digital image correlation by feature-based method,' Optics and Lasers in Engineering, 2018, **104**, pp. 149–158.

[26] Zhang, Z., Hauge, M., Ødegård, J., and Thaulow, C., 'Determining material true stress–strain curve from tensile specimens with rectangular cross-section,' International Journal of Solids and Structures, 1999, **36**(23), pp. 3497–3516.

[27] Zhao, Y., Guo, Y., Wei, Q., Topping, T., Dangelewicz, A., Zhu, Y., Langdon, T., and Lavernia, E., 'Influence of specimen dimensions and strain measurement methods on tensile stress–strain curves,' Materials Science and Engineering: A, 2009, **525**(1-2), pp. 68–77.

[28] Zhu, F., Bai, P., Zhang, J., Lei, D., and He, X., 'Measurement of true stress–strain curves and evolution of plastic zone of low carbon steel under uniaxial tension using digital image correlation,' Optics and Lasers in Engineering, 2015, **65**, pp. 81–88.

SECTION

2. CONCLUSION AND FUTURE WORK

2.1. CONCLUSION

In this research, the accuracy and efficiency of DIC method have been improved. It has been applied to the miniature mechanical test as a non-contact metrology technique. Special attention has been paid in addressing the practical issues in the used of DIC for material mechanical test.

A new feature matching based method was proposed to provide more accurate pixel level searching result. The FB-IG scheme combines the FG-GMM point set registration algorithm and the ORB feature extractor in the pixel level searching stage of DIC. Extracted features are semi-uniformly distributed in ROI by the clustering method. The global continues deformation field is interpolated on feature points in the reference image by the RKHS function. After solving the optimization problem by the EM algorithm, correct feature pairs and nonuniform deformation field are determined simultaneously. Validations on simulated images and real-world mini tensile test verify that this scheme can robustly and accurately compute initial guesses with semi-subpixel level accuracy in cases with small or large translation, deformation, or rotation.

The simple but effective BS strategy was presented to automatically update the reference frames in the DIC analysis. The frame step is reduced into one half for the unconverged locations, and the intermediate frame is utilized to assist the correlating process. This process is iteratively conducted to adjust the frame step in different regions automatically. The performance of the BS strategy is evaluated against the CS update strategy on simulated experiments. The results indicate that the BS strategy can automatically adjust

the frame step for changing speckle pattern and loading rate. The accuracy and robustness of the BS strategy are better than the CS strategy with the same pixel level and subpixel level searching algorithms. The BS strategy also successfully tracked all POIs and adjusted the frame step in the real world experiment with changing loading rate and large plastic deformation (over 70% engineering strain).

A new convenient experimental method to determine the true stress-strain curve from the miniature tensile test was proposed. The new miniature tensile specimen with a parallel section of $3 \times 1 \times 1$ mm was used. The 1:1 width-to-thickness ratio enables the estimation of cross-section area by only one camera, and the telecentric lens can eliminate the effect of out-of-plane motion. The derived true stress-strain curves and mechanical parameters of Al6061 and CPTi from miniature specimens match well with the results of standard specimens. No dimension dependence has been observed in the results. FEA simulation was used to evaluate the correctness of the derived true stress-strain curve. The maximum deviation of the simulated and experimental load is only 2-3%. The result shows that the derived true stress-strain curve is capable to represent the constitutive behavior of the tested materials.

2.2. FUTURE WORK

The present research has shown the great potential of optical metrology method DIC in the area of miniature mechanical test. Much improvement can still be done to improve the DIC algorithm itself and miniature experiment technique. The following suggestions can be carried out to deepen the research subject:

- In most real applications of DIC, the speckle pattern was generated by spray painting or airbrushing. Although the resulted speckle pattern usually could fulfill the practical requirements, a carefully designed pattern with optimal distribution and size of the speckles will increase the accuracy of the measured results.

- Although the BS strategy solved the problem of selecting proper reference frames in DIC, and the resulted accumulated error is reduced. The basic process is essentially pairwise, e.g., the displacement for a POI from frame i to frame j is calculated from these two frames if no decorrelation occurs. A new strategy can be adopted to further increase the accuracy of DIC by utilizing other frames besides frame i and j. How to integrate the results from different routes and select the intermediate frames deserve further study.

- In the current study, isotropic material and isotropic hardening are assumed to derive the true stress-strain curve. The limitation can be overcome by introducing more comprehensive material model and additional cameras.

- In addition to the miniature tensile test, other type of miniature test, such as compression, bending, and fatigue, can be incorporated with DIC to simplify the experimental implementation and expand to high speed, high temperature, and other environments.

REFERENCES

[1] Aronszajn, N., 'Theory of reproducing kernels,' Transactions of the American mathematical society, 1950, **68**(3), pp. 337–404, ISSN 0002-9947.

[2] Bay, H., Ess, A., Tuytelaars, T., and Van Gool, L., 'Speeded-up robust features (surf),' Computer vision and image understanding, 2008, **110**(3), pp. 346–359.

[3] Blaber, J., Adair, B., and Antoniou, A., 'Ncorr: open-source 2d digital image correlation matlab software,' Experimental Mechanics, 2015, **55**(6), pp. 1105–1122.

[4] Bridgman, P. W., *Studies in large plastic flow and fracture*, volume 177, McGraw-Hill New York, 1952.

[5] Bruck, H. A., McNeill, S. R., Sutton, M. A., and Peters, W. H., 'Digital image correlation using Newton-Raphson method of partial differential correction,' Experimental mechanics, 1989, **29**(3), pp. 261–267, ISSN 0014-4851.

[6] Calonder, M., Lepetit, V., Strecha, C., and Fua, P., 'Brief: Binary robust independent elementary features,' in 'European conference on computer vision,' Springer, 2010 pp. 778–792.

[7] Chen, F., Chen, S., Dong, X., Li, C., Hong, X., and Zhang, X., 'Size effects on tensile strength of aluminum–bronze alloy at room temperature,' Materials & Design, 2015, **85**, pp. 778–784.

[8] Chen, Z., Shao, X., Xu, X., and He, X., 'Optimized digital speckle patterns for digital image correlation by consideration of both accuracy and efficiency,' Applied optics, 2018, **57**(4), pp. 884–893.

[9] Chi, Y. and Pan, B., 'Spatial-temporal subset-based digital image correlation: A general framework,' CoRR, 2018, **abs/1812.04826**.

[10] Choung, J. and Cho, S., 'Study on true stress correction from tensile tests,' Journal of Mechanical Science and Technology, 2008, **22**(6), pp. 1039–1051.

[11] De Strycker, M., Schueremans, L., Van Paepegem, W., and Debruyne, D., 'Measuring the thermal expansion coefficient of tubular steel specimens with digital image correlation techniques,' Optics and Lasers in Engineering, 2010, **48**(10), pp. 978–986, ISSN 0143-8166.

[12] Eberl, C., Gianola, D. S., and Hemker, K. J., 'Mechanical characterization of coatings using microbeam bending and digital image correlation techniques,' Experimental mechanics, 2010, **50**(1), pp. 85–97, ISSN 0014-4851.

[13] Eshtayeh, M., Hijazi, A., and Hrairi, M., 'Nondestructive Evaluation of Welded Joints Using Digital Image Correlation,' Journal of Nondestructive Evaluation, 2015, **34**(4), pp. 1–12, ISSN 1573-4862, doi:10.1007/s10921-015-0310-z.

[14] Geringer, J. and Katoh, Y., 'Atf neutron irradiation program technical plan,' Technical report, Oak Ridge National Lab.(ORNL), 2016.

[15] Goh, C., Ismail, H., Yen, K., and Ratnam, M., 'Single-step scanner-based digital image correlation (sb-dic) method for large deformation mapping in rubber,' Optics and Lasers in Engineering, 2017, **88**, pp. 167–177.

[16] Grant, B. M. B., Stone, H. J., Withers, P. J., and Preuss, M., 'High-temperature strain field measurement using digital image correlation,' The Journal of Strain Analysis for Engineering Design, 2009, **44**(4), pp. 263–271, ISSN 0309-3247.

[17] Gussev, M., Busby, J., Field, K., Sokolov, M., and Gray, S., 'Role of scale factor during tensile testing of small specimens,' in 'Small Specimen Test Techniques: 6th Volume,' ASTM International, 2015.

[18] Gussev, M. N., Howard, R. H., Terrani, K. A., and Field, K. G., 'Sub-size tensile specimen design for in-reactor irradiation and post-irradiation testing,' Nuclear Engineering and Design, 2017, **320**, pp. 298–308.

[19] Horaud, R., Forbes, F., Yguel, M., Dewaele, G., and Zhang, J., 'Rigid and articulated point registration with expectation conditional maximization,' IEEE Transactions on Pattern Analysis and Machine Intelligence, 2011, **33**(3), pp. 587–602.

[20] Jaya, N. B. and Alam, M. Z., 'Small-scale mechanical testing of materials,' Current Science, 2013, **105**(8), pp. 1073–1099.

[21] Kamaya, M. and Kawakubo, M., 'True stress–strain curves of cold worked stainless steel over a large range of strains,' Journal of Nuclear Materials, 2014, **451**(1-3), pp. 264–275.

[22] Kamaya, M., Kitsunai, Y., and Koshiishi, M., 'True stress–strain curve acquisition for irradiated stainless steel including the range exceeding necking strain,' Journal of Nuclear Materials, 2015, **465**, pp. 316–325.

[23] Karnati, S., Zhang, Y., Liou, F. F., and Newkirk, J. W., 'On the feasibility of tailoring copper–nickel functionally graded materials fabricated through laser metal deposition,' Metals, 2019, **9**(3), p. 287.

[24] Kim, J.-H., Serpantié, A., Barlat, F., Pierron, F., and Lee, M.-G., 'Characterization of the post-necking strain hardening behavior using the virtual fields method,' International Journal of Solids and Structures, 2013, **50**(24), pp. 3829–3842.

[25] Kim, Y. S., Hofman, G., Robinson, A., Snelgrove, J., and Hanan, N., 'Oxidation of aluminum alloy cladding for research and test reactor fuel,' Journal of Nuclear Materials, 2008, **378**(2), pp. 220–228.

[26] Kohno, Y., Kohyama, A., Hamilton, M. L., Hirose, T., Katoh, Y., and Garner, F. A., 'Specimen size effects on the tensile properties of jpca and jfms,' Journal of nuclear materials, 2000, **283**, pp. 1014–1017.

[27] Kumar, K., Pooleery, A., Madhusoodanan, K., Singh, R., Chakravartty, J., Dutta, B., and Sinha, R., 'Use of miniature tensile specimen for measurement of mechanical properties,' Procedia Engineering, 2014, **86**, pp. 899–909.

[28] Kumar, K., Pooleery, A., Madhusoodanan, K., Singh, R., Chatterjee, A., Dutta, B., and Sinha, R., 'Optimisation of thickness of miniature tensile specimens for evaluation of mechanical properties,' Materials Science and Engineering: A, 2016, **675**, pp. 32–43.

[29] LaVan, D., 'Microtensile properties of weld metal,' Experimental techniques, 1999, **23**(3), pp. 31–34.

[30] Le Roy, G., Embury, J., Edwards, G., and Ashby, M., 'A model of ductile fracture based on the nucleation and growth of voids,' Acta Metallurgica, 1981, **29**(8), pp. 1509–1522.

[31] Lewis, J. P., 'Fast normalized cross-correlation,' in 'Vision interface,' volume 10, 1995 pp. 120–123.

[32] Liu, H., Shen, Y., Yang, S., Zheng, P., and Zhang, L., 'A comprehensive solution to miniaturized tensile testing: Specimen geometry optimization and extraction of constitutive behaviors using inverse fem procedure,' Fusion Engineering and Design, 2017, **121**, pp. 188–197.

[33] Lowe, D. G., 'Object recognition from local scale-invariant features,' in 'Computer vision, 1999. The proceedings of the seventh IEEE international conference on,' volume 2, Ieee, 1999 pp. 1150–1157.

[34] Luo, P., Chao, Y., Sutton, M., and Peters, W.-H., 'Accurate measurement of three-dimensional deformations in deformable and rigid bodies using computer vision,' Experimental mechanics, 1993, **33**(2), pp. 123–132.

[35] Ma, J., Jiang, J., Gao, Y., Chen, J., and Liu, C., 'Robust image matching via feature guided Gaussian mixture model,' 2016 IEEE International Conference on Multimedia and Expo (ICME), 2016, pp. 1–6, doi:10.1109/ICME.2016.7552867.

[36] Ma, S., Zhao, Z., and Wang, X., 'Mesh-based digital image correlation method using higher order isoparametric elements,' The Journal of Strain Analysis for Engineering Design, 2012, **47**(3), pp. 163–175, ISSN 0309-3247.

[37] Mahabunphachai, S. and Koç, M., 'Investigations on forming of aluminum 5052 and 6061 sheet alloys at warm temperatures,' Materials & Design (1980-2015), 2010, **31**(5), pp. 2422–2434.

[38] Matthews, L., Ishikawa, T., and Baker, S., 'The template update problem,' IEEE transactions on pattern analysis and machine intelligence, 2004, **26**(6), pp. 810–815.

[39] Mekky, W. and Nicholson, P. S., 'The fracture toughness of Ni/Al2O3 laminates by digital image correlation I: Experimental crack opening displacement and R-curves,' Engineering Fracture Mechanics, 2006, **73**(5), pp. 571–582, ISSN 00137944, doi: 10.1016/j.engfracmech.2005.09.005.

[40] Myronenko, A. and Song, X., 'Point set registration: Coherent point drift,' IEEE transactions on pattern analysis and machine intelligence, 2010, **32**(12), pp. 2262–2275.

[41] Pan, B., 'Reliability-guided digital image correlation for image deformation measurement,' Applied optics, 2009, **48**(8), pp. 1535–1542.

[42] Pan, B., 'Recent progress in digital image correlation,' Experimental Mechanics, 2011, **51**(7), pp. 1223–1235.

[43] Pan, B., 'An evaluation of convergence criteria for digital image correlation using inverse compositional gauss–newton algorithm,' Strain, 2014, **50**(1), pp. 48–56.

[44] Pan, B., 'Digital image correlation for surface deformation measurement: historical developments, recent advances and future goals,' Measurement Science and Technology, 2018, **29**(8), p. 082001.

[45] Pan, B., Dafang, W., and Yong, X., 'Incremental calculation for large deformation measurement using reliability-guided digital image correlation,' Optics and Lasers in Engineering, 2012, **50**(4), pp. 586–592.

[46] Pan, B., Li, K., and Tong, W., 'Fast, Robust and Accurate Digital Image Correlation Calculation Without Redundant Computations,' Experimental Mechanics, 2013, **53**(7), pp. 1277–1289, ISSN 1741-2765, doi:10.1007/s11340-013-9717-6.

[47] Pan, B., Li, K., and Tong, W., 'Fast, robust and accurate digital image correlation calculation without redundant computations,' Experimental Mechanics, 2013, **53**(7), pp. 1277–1289.

[48] Pan, B., Qian, K., Xie, H., and Asundi, A., 'Two-dimensional digital image correlation for in-plane displacement and strain measurement: a review,' Measurement science and technology, 2009, **20**(6), p. 62001, ISSN 0957-0233.

[49] Pan, B., Qian, K., Xie, H., and Asundi, A., 'Two-dimensional digital image correlation for in-plane displacement and strain measurement: a review,' Measurement science and technology, 2009, **20**(6), p. 062001.

[50] Pan, B., Wang, B., and Lubineau, G., 'Comparison of subset-based local and fe-based global digital image correlation: Theoretical error analysis and validation,' Optics and Lasers in Engineering, 2016, **82**, pp. 148–158.

[51] Pan, B., Wu, D., Wang, Z., and Xia, Y., 'High-temperature digital image correlation method for full-field deformation measurement at 1200 C,' Measurement science and technology, 2010, **22**(1), p. 15701, ISSN 0957-0233.

[52] Pan, B., Xie, H., and Wang, Z., 'Equivalence of digital image correlation criteria for pattern matching,' Applied optics, 2010, **49**(28), pp. 5501–5509.

[53] Pan, B., Xie, H., Xu, B., and Dai, F., 'Performance of sub-pixel registration algorithms in digital image correlation,' Measurement Science and Technology, 2006, **17**(6), p. 1615.

[54] Peters, W. H. and Ranson, W. F., 'Digital Imaging Techniques In Experimental Stress Analysis,' Optical Engineering, 1982, **21**(3), pp. 213427–213427, ISSN 0091-3286.

[55] Ramchandran, D., Kumar, A., Chaitanya, G., Karthik, V., and Kolhatkar, A., 'Development and validation of a miniature tensile specimen for determination of mechanical properties,' Journal of Testing and Evaluation, 2019, **47**(5).

[56] Rosten, E. and Drummond, T., 'Machine learning for high-speed corner detection,' in 'European conference on computer vision,' Springer, 2006 pp. 430–443.

[57] Rublee, E., Rabaud, V., Konolige, K., and Bradski, G., 'Orb: An efficient alternative to sift or surf,' in 'Computer Vision (ICCV), 2011 IEEE International Conference on,' IEEE, 2011 pp. 2564–2571.

[58] Sánchez-Arévalo, F. and Pulos, G., 'Use of digital image correlation to determine the mechanical behavior of materials,' Materials Characterization, 2008, **59**(11), pp. 1572–1579, ISSN 10445803, doi:10.1016/j.matchar.2008.02.002.

[59] Scheider, I., Brocks, W., and Cornec, A., 'Procedure for the determination of true stress-strain curves from tensile tests with rectangular cross-section specimens,' Journal of engineering materials and technology, 2004, **126**(1), pp. 70–76.

[60] Sedaghat, A., Mokhtarzade, M., and Ebadi, H., 'Uniform robust scale-invariant feature matching for optical remote sensing images,' IEEE Transactions on Geoscience and Remote Sensing, 2011, **49**(11), pp. 4516–4527.

[61] Su, Y., Zhang, Q., Fang, Z., Wang, Y., Liu, Y., and Wu, S., 'Elimination of systematic error in digital image correlation caused by intensity interpolation by introducing position randomness to subset points,' Optics and Lasers in Engineering, 2019, **114**, pp. 60–75.

[62] Sun, Y., Pang, J. H. L., Wong, C. K., and Su, F., 'Finite element formulation for a digital image correlation method,' Applied optics, 2005, **44**(34), pp. 7357–7363, ISSN 1539-4522.

[63] Sur, F., Blaysat, B., and Grediac, M., 'Rendering deformed speckle images with a boolean model,' Journal of Mathematical Imaging and Vision, 2017, pp. 1–17.

[64] Sutton, M. A., 'Computer vision-based, noncontacting deformation measurements in mechanics: a generational transformation,' Applied Mechanics Reviews, 2013, **65**(5), p. 050802.

[65] Tang, Z., Liang, J., Xiao, Z., and Guo, C., 'Large deformation measurement scheme for 3d digital image correlation method,' Optics and Lasers in Engineering, 2012, **50**(2), pp. 122–130.

[66] Tsai, D.-M. and Lin, C.-T., 'Fast normalized cross correlation for defect detection,' Pattern Recognition Letters, 2003, **24**(15), pp. 2625–2631, ISSN 0167-8655.

[67] Verstraete, M., Denys, R., Van Minnebruggen, K., Hertelé, S., and De Waele, W., 'Determination of CTOD resistance curves in side-grooved Single-Edge Notched Tensile specimens using full field deformation measurements,' Engineering Fracture Mechanics, 2013, **110**, pp. 12–22, ISSN 00137944, doi:10.1016/j.engfracmech.2013.07.015.

[68] Wang, B., Pan, B., and Lubineau, G., 'Some practical considerations in finite element-based digital image correlation,' Optics and Lasers in Engineering, 2015, **73**, pp. 22–32.

[69] Wang, H., Xu, T., and Shou, B., 'Determination of material strengths by hydraulic bulge test,' Materials, 2017, **10**(1), p. 23.

[70] Wang, Z., Vo, M., Kieu, H., and Pan, T., 'Automated Fast Initial Guess in Digital Image Correlation,' Strain, 2014, **50**(1), pp. 28–36, ISSN 00392103, doi:10.1111/str.12063.

[71] Wu, R., Kong, C., Li, K., and Zhang, D., 'Real-time digital image correlation for dynamic strain measurement,' Experimental Mechanics, 2016, **56**(5), pp. 833–843.

[72] Yazzie, K., Williams, J., and Chawla, N., 'Quantifying necking of rectangular tensile specimens using a mirror-based image analysis system,' Materials Letters, 2012, **74**, pp. 243–246.

[73] Zhang, Y., Xie, X., Wang, X., Li, Y., and Ling, X., 'Adaptive image mismatch removal with vector field interpolation based on improved regularization and gaussian kernel function,' IEEE Access, 2018, **6**, pp. 55599–55613, ISSN 2169-3536, doi: 10.1109/ACCESS.2018.2871743.

[74] Zhang, Y., Yan, L., Karnati, S., and Liou, F., 'Bisection searching based reference frame update strategy for digital image correlation,' SN Applied Sciences, 2019, **1**(6), p. 588.

[75] Zhang, Y., Yan, L., and Liou, F., 'Improved initial guess with semi-subpixel level accuracy in digital image correlation by feature-based method,' Optics and Lasers in Engineering, 2018, **104**, pp. 149–158.

[76] Zhang, Z., Hauge, M., Ødegård, J., and Thaulow, C., 'Determining material true stress–strain curve from tensile specimens with rectangular cross-section,' International Journal of Solids and Structures, 1999, **36**(23), pp. 3497–3516.

[77] Zhao, J.-q., Zeng, P., Lei, L.-p., and Ma, Y., 'Initial guess by improved population-based intelligent algorithms for large inter-frame deformation measurement using digital image correlation,' Optics and Lasers in Engineering, 2012, **50**(3), pp. 473–490.

[78] Zhao, Y., Guo, Y., Wei, Q., Topping, T., Dangelewicz, A., Zhu, Y., Langdon, T., and Lavernia, E., 'Influence of specimen dimensions and strain measurement methods on tensile stress–strain curves,' Materials Science and Engineering: A, 2009, **525**(1-2), pp. 68–77.

[79] Zhou, Y. and Chen, Y. Q., 'Feature matching for automated and reliable initialization in three-dimensional digital image correlation,' Optics and Lasers in Engineering, 2013, **51**(3), pp. 213–223, ISSN 01438166, doi:10.1016/j.optlaseng.2012.10.011.

[80] Zhou, Y., Pan, B., and Chen, Y. Q., 'Large deformation measurement using digital image correlation: a fully automated approach,' Applied optics, 2012, **51**(31), pp. 7674–7683, ISSN 1539-4522.

[81] Zhou, Y., Sun, C., and Chen, J., 'Adaptive subset offset for systematic error reduction in incremental digital image correlation,' Optics and Lasers in Engineering, 2014, **55**, pp. 5–11.

[82] Zhu, F., Bai, P., Zhang, J., Lei, D., and He, X., 'Measurement of true stress–strain curves and evolution of plastic zone of low carbon steel under uniaxial tension using digital image correlation,' Optics and Lasers in Engineering, 2015, **65**, pp. 81–88.

VITA

Yunlu Zhang was born in Sichuan, China. He received his bachelor of science degree in Material Science and Engineering in June 2010 from Shanghai Jiaotong University, Shanghai, China. In January 2013, he received his master of science degree in Material Science and Engineering from Shanghai Jiaotong University, Shanghai, China. In December 2019, he received his doctor of philosophy in Mechanical Engineering from Missouri University of Science and Technology, Rolla, Missouri, USA. His research focused on metal additive manufacturing, functional gradient material, optical metrology, and mechanical testing of materials. He authored and co-authored ten journal papers and seven conference papers in the metal additive manufacturing and mechanical testing areas.